Available online at www.sciencedirect.com
SCIENCE DIRECT®
Journal of Molecular Spectroscopy 228 (2004) 121–142
Journal of MOLECULAR SPECTROSCOPY
www.elsevier.com/locate/jms

Self- and foreign-gas-broadened lineshapes in the v_1 band of NH_3

A.S. Pine[a,*], V.N. Markov[b]

[a] Alpine Technologies, 14401 Poplar Hill Road, Germantown, MD 20874, USA
[b] Applied Physics Institute, Russian Academy of Sciences, Uljanova Street 46, Nizhnii Novgorod 603600, Russia

Received 5 April 2004; in revised form 29 June 2004

Abstract

Precise N_2, O_2, H_2, Ar, He, and self-broadenings and shifts have been obtained for Q- and R-branch transitions in the v_1 fundamental band of ammonia from simultaneous fits of low-noise, high-resolution difference-frequency laser spectra at pressures from 0.07 to 27 kPa (0.5–200 Torr). Observed lineshapes exhibit significant deviations from the conventional Voigt profile, which may be attributed to Dicke narrowing and/or speed-dependent broadening. At the higher pressures, line mixing is evident and must be included in the fits. For self-broadening, line mixing is dominated by collisional tunneling transitions, whereas for the non-polar buffers, rotational relaxation among selected K states is the primary mixing mechanism.

Keywords: NH_3; Self- and foreign-gas broadening and shifts; Dicke narrowing; Speed dependence; Line mixing; Line intensities

1. Introduction

In an earlier study of self-broadening [1] of NH_3, we recorded high-resolution difference-frequency laser spectra of the Q branch and $R(0,0)$, $R(1,K)$, and $R(3,K)$ manifolds in the v_1 fundamental band at pressures up to 13.3 kPA (100 Torr). Least-squares fits were performed on individual spectra at lower pressures ($\leqslant$20 Torr) where the lines were not too severely overlapped. Voigt lineshapes were utilized to obtain the broadenings, though deviations which could be attributed to Dicke narrowing were observed for the R-branch lines. The v_1 self-broadenings agreed well with prior ground-state microwave and v_2 ladder measurements, showed excellent consistency for tunneling pairs, and exhibited a strong J and K dependence in qualitative accord with semiclassical line broadening calculations based purely on dipole–dipole interactions. The higher pressure measurements showed significant discrepancies from spectra calculated from the broadening and shift coefficients determined at lower pressure, indicating line mixing; but this was not investigated further.

Foreign-gas broadening [2] of NH_3 was also studied in the same spectral regions for N_2, O_2, H_2, Ar, and He buffers for application to atmospheric monitoring of the earth and outer planets. Here, Dicke narrowing was required to fit the lineshapes as the Voigt profile generally exhibited large systematic residuals. The Dicke-narrowing coefficients were obtained from hard-collision Rautian [3] or soft-collision Galatry [4] profile fits to just the 50 Torr traces where they were best determined. These narrowing coefficients were in rough correspondence with the values expected from diffusion,

$$\beta_d = k_B T/2\pi c M_a D_{ab}. \quad (1)$$

Here k_B is the Boltzmann constant, T is the temperature, c is the speed of light, M_a is the mass of the absorbing molecule, and D_{ab} is the binary mass diffusion constant for the collision partners. Projected spectra at the higher pressures (100 and 200 Torr) measured also showed line-mixing discrepancies which, however, were considerably smaller than for self-broadening. The observed $J-K$

* Corresponding author.
E-mail address: alanpine@erols.com (A.S. Pine).

0022-2852/$ - see front matter © 2004 Elsevier Inc. All rights reserved.
doi:10.1016/j.jms.2004.07.007

dependence of the foreign-gas broadening coefficients for the Q branch were also much smaller than for self-broadening or for model calculations. The observed rotational dependence in the R branch was in better agreement with the calculations.

In the present work, we reexamine the same data [1,2] using a multiple-spectrum fitting procedure [5–8], which has been demonstrated to permit overlapped lines to be distinguished, to yield line-mixing parameters, to allow baselines to be automatically adjusted, and to improve the parameter precision by reducing parameter correlation and increasing the amount of data fit. Self-broadening corrections, ignored previously [2], are included here for the dilute mixtures with foreign-gas buffers. We also test the effect of speed-dependent broadening [6–11] on the lineshapes and its possible confusion with Dicke narrowing. Our earlier studies [1,2] were calibrated against the FTS ammonia spectrum of Angstl et al. [12] and used the assignments from their perturbation analysis. Subsequently, the NH_3 spectral calibration has been improved and the assignments extended by Kleiner et al. [13], whose results are now included in the HITRAN2K database [14]. Therefore, we recalibrate our results in accord with this database, though we still find a number of weak lines unassigned and a few predicted lines unobserved. Moreover, we can curve resolve many blended lines with multiple assignments, and find a systematic discrepancy in the line intensities. Finally, we compare our broadenings with some recent FTS measurements in other parallel bands of NH_3 [15,16] for some indication of the vibrational and tunneling dependence of the linewidths. Comparisons with earlier studies were made in our previous reports [1,2].

2. Experimental considerations

The pressure-broadened ammonia ν_1 band Q- and R-branch spectra near 3 μm were recorded with a linear-scan-controlled difference-frequency laser as described in the previous reports [1,2]. The ammonia sample was of commercial anhydrous grade (nominal purity ⩾99.99%) with natural isotopic composition. A 51 cm cell was used for the low pressure, $P \cong 0.5$ Torr (1 atm = 760 Torr = 101 325 Pa) traces, which were included in all the multifits to establish a wavenumber reference for the pressure shifts. The near-Doppler-limited Q-branch traces are shown in [1], labeled with the assignments [12] of the stronger lines. A shorter 5.8 cm cell was used for the self-broadening measurements ($P \cong 5$, 10, 20, 50, and 100 Torr) with a 0.5 liter ballast bulb to help stabilize the pressures during the 5 min scans. The foreign-gas-broadening measurements used a double-passed 191 cm cell with a nominal NH_3 concentration of 0.5%, premixed in an electropolished stainless steel 6 liter chamber. The premixed gases were introduced into the cell at $P \cong 200$ Torr and pumped down for the subsequent scans at $P \cong 100$, 50, 20, and 10 Torr. Small variations in the mixture concentration due to wall adsorption were observed in the measured intensities. The cells were glass with CaF_2 windows mounted at Brewster's angle to minimize channeling. In most cases, an empty cell trace was recorded to normalize the baselines against some interference fringes and atmospheric water vapor lines and to provide an initial estimate for the strongly overlapped traces at higher pressures. Pressures were measured with capacitance manometers, nominally accurate to 0.5%. Self-broadening measurements were made at $T = 297(1)$ K and foreign-gas broadening at $T = 296(1)$ K.

3. Fitting procedure

The observed transmission traces at different pressures are simultaneously fit to calculated spectra of the form:

$$\Upsilon(\omega) = \int_{-\infty}^{+\infty} I(\omega - \omega')B(\omega') \times \exp\left[-C_a PL \sum_m S_m R_m(\omega')\right] d\omega' + Z_{off}. \quad (2)$$

Here, $I(\omega - \omega')$ is the instrumental function, $B(\omega)$ is the baseline or empty cell transmission, C_a is the concentration of the active species, P is the total pressure, L is the cell length, S_m is the transition intensity, $R_m(\omega)$ is the normalized lineshape or profile, and Z_{off} represents any instrumental zero offset. In general, the index m labels all species and vibrational and rotational quantum numbers for any line in the spectrum. The exponential function represents Beer's law, and the linear sum over individual line contributions is only valid when line mixing can be ignored or treated in first order [17].

For the difference-frequency laser, $I(\omega - \omega')$ depends on the jitter-induced linewidth (∼1 MHz FWHM), which is negligible compared to the Doppler width (∼300 MHz FWHM for ν_1 of NH_3 at $T = 296$ K), and the effective time constant (∼65 ms) and scan rate (0.0125 cm^{-1}/s). Contributions to the baseline, $B(\omega)$, can be fit to a polynomial in ω for slow source or detector variations, with sine functions for window or filter channeling, and with Lorentzian functions for extraneous atmospheric absorptions in the beam path [6]. These NH_3 spectra are fit in segments of 6000 data points covering 3.75 cm^{-1}. Over this range, a cubic polynomial and one interference channel with a period of ∼1.5 cm^{-1} are generally sufficient for the baseline. An occasional atmospheric water line is included for those traces not normalized with an empty cell baseline. While the empty cell trace normalization tends to flatten the baseline, it also increases the noise by $\sqrt{2}$. It does not compensate

for fringes that drift in time or from refractive angular displacement of the beam. A few lines outside the fitting range are kept in the calculations if their wings affect the fitted baseline. The zero offset appears to be negligible ($\leqslant 0.1\%$) in this data set; so we set $Z_{\rm off} = 0$.

The integrated line intensities, S_m, are fit only for the self-broadened traces where the pressures are monitored during the scan and unity concentration is assured. The pressure is adjusted for the closed-cell Doppler-limited traces to be in conformance with the self-broadened scans in the simultaneous fits. For the multifits of the foreign-gas mixtures, the S_m are fixed to the self-broadened values and the concentrations, $C_{\rm a}$, were floated; they varied by a few percent due to wall adsorption. Because the self-broadenings can be from ~2.5 to 25 times larger than the foreign-gas broadenings, depending on the buffer and transition, the self-contribution to the measured broadenings are several percent for the ~0.5% mixture concentration. We correct the observed broadenings using

$$\gamma_m = C_{\rm a}\gamma_m^{\rm self} + (1 - C_{\rm a})\gamma_m^{\rm buffer}. \tag{3}$$

This correction was neglected in the earlier report [2], so the foreign-gas broadenings there are systematically high by ~2% for N_2 to ~10% for He.

Since the foreign-gas scans were recorded with different cells on different days from the self-broadened and Doppler-limited traces, we allow for calibration shifts of the buffer gas traces. These calibration shifts are found to be $0.00013(8)\,{\rm cm}^{-1}$ and are constrained to be equal for all runs of a given buffer gas in order to yield reliable transition pressure shifts. Once the zero-pressure transition wavenumbers are determined for the self-broadening data, they are held fixed in the multifits for the foreign-gas buffers. An overall shift of each manifold is applied after the fitting analysis to recalibrate relative to the newer database [13,14].

4. Lineshape models

For the analysis of these NH_3 spectra, the most general lineshape we consider is the speed-dependent, dispersive Rautian (sdR) profile [3,6–8,18,19]

$$R_m(\omega) = (1/\pi)\,{\rm Re}\{[1 + {\rm i}\zeta_m]F_m(\omega)/[1 - \beta_m F_m(\omega)]\}, \tag{4}$$

where

$$F_m(\omega) = \int {\rm d}\mathbf{v} W_M(\mathbf{v})/[\beta_m + \gamma_m(v) - {\rm i}(\omega - \omega_m - \delta_m(v) - \mathbf{k}\cdot\mathbf{v})]. \tag{5}$$

Here ζ_m is the dispersion parameter representative of first-order line mixing [17–19], β_m is the Dicke-narrowing parameter for the hard-collision model [3], $\gamma_m(v)$ and $\delta_m(v)$ are the speed-dependent broadening and shift [9–11], where v is the speed of the absorbing molecule with velocity $\mathbf{v}$, $\mathbf{k} = (\omega/c)\hat{k}$ is the wavevector of the optical probe taken at some representative wavenumber, ω, and $W_M(\mathbf{v})$ is the Maxwellian velocity distribution,

$$W_M(\mathbf{v}) = \left(\sqrt{\pi}\overline{v}\right)^{-3}\exp\left(-v^2/\overline{v}^2\right), \quad \overline{v} = \sqrt{2k_{\rm B}T/M_{\rm a}}. \tag{6}$$

In the binary collision regime, the ζ, β, γ, and δ parameters are all implicitly linear in pressure. We fit, however, for their respective pressure coefficients, denoted by the same labels as the parameters.

This sdR profile reduces to the speed-dependent, dispersive Voigt (sdV) profile [9,10,20] if Dicke narrowing is ignored ($\beta_m = 0$). When the broadening and shift do not depend on speed, the sdR profile becomes the dispersive Rautian (dR) [3,21], with

$$F_m(\omega) \Rightarrow \left(\sqrt{\pi}/\sigma\right)w((\omega - \omega_m - \delta_m)/\sigma + {\rm i}(\gamma_m + \beta_m)/\sigma), \tag{7}$$

where $w(x + {\rm i}y)$ is the complex probability function (for which there are efficient algorithms [22]) and $\sigma = \omega_m\overline{v}/c$ is the Doppler half width at $1/e$ intensity. The dispersive Voigt (dV) profile is obtained if both Dicke narrowing and speed dependence are ignored, and the conventional Voigt (V) results if line mixing is also neglected.

For isolated lines, the form of $R_m(\omega)$ above was derived by Rautian and Sobel'man [3] for "statistically independent" velocity-changing and dephasing collisions, where the velocity-changing collision rate is measured by diffusion, $\beta = \beta_{\rm d}$. They also showed for "statistically dependent" collisions, $\gamma + {\rm i}\delta$ should be subtracted from $\beta_{\rm d}$. For partial correlations, we use an effective narrowing parameter,

$$\beta = \beta_{\rm d} - \eta_\gamma\gamma - {\rm i}\eta_\delta\delta, \tag{8}$$

where the η represent the fraction of dephasing collisions that are also velocity-changing [18]. For simplicity, we ignore the speed dependence of β here, though in principle all these parameters may be functions of v [18]. Since γ and δ may also depend on the particular transition, so may β, though this presents some mathematical difficulties in the line-mixing matrix inversion [19]. In addition to the hard-collision profile above, we have also tested analogous soft-collision profiles [2,4,18] and found similar quality fits for most of our NH_3 spectra. The speed-dependent soft-collision models [18] are slower computationally and require more memory.

Ideally, the speed dependence of the broadenings and shifts can be calculated either semiclassically or quantum-mechanically from realistic interaction potentials. However, this has been done for only a few simple cases such as HF-Ar [23,24] and CO-Ar [25]. Therefore, we use the classical-path R^{-q} potential model of Berman [9] and Ward et al. [10]. This yields broadenings and shifts in terms of the confluent hypergeometric function [26],

$$\frac{\gamma(v)}{\langle\gamma\rangle} = \frac{\delta(v)}{\langle\delta\rangle} = (1+\varrho)^{-p/2} M\left(-\frac{p}{2}, \frac{3}{2}, -\varrho\frac{v^2}{\overline{v}^2}\right), \tag{9}$$

where the angle brackets denote the thermal average, $\varrho = M_b/M_a$ where M_b is the mass of the perturber ($\varrho = 1$ for self-broadening), and $p = (q-3)/(q-1)$. The fits are refined for $\langle\gamma\rangle$, $\langle\delta\rangle$, and the range parameter q. The speed dependence of the shifts can lead to an asymmetry of the line profile [9,10,24], which is not observable here due to the small shifts relative to the widths. The connection between the speed dependencies of the shifts and broadenings is a consequence of the pure dephasing model for an isotropic potential. Pickett [27] has generalized this model to find a different effective value of $p_\delta \approx -3/(q-1)$ for the shifts. A simple quadratic speed dependence has also been used for CO in O_2 and N_2 [11],

$$\gamma(v)/\langle\gamma\rangle = 1 + \tilde{q}\left[(v/\overline{v})^2 - 3/2\right]. \tag{10}$$

Though this form is not derivable from a potential, it has convenient analytical properties [11], and we also test its applicability here.

5. Dicke narrowing and speed-dependent broadening

The collisional mechanisms contributing to the NH_3 lineshapes are well illustrated with the multifits to the $R(3,K)$ manifold of the ν_1 fundamental band. Fig. 1 shows the observed 50 Torr Ar-broadened $sqR(3,K)$ transitions from the ground-state symmetric tunneling level. Several ν_3 fundamental band transitions, denoted by asterisks, are interposed. The fitted dispersive Rautian, dR, with no speed dependence, is overlaid with dots and the 5× magnified observed–calculated residuals are almost within the noise level of the measurement. The magnified residuals for other models are offset for visibility. The noticeable residuals for the ν_3 band line near 3414.97 cm^{-1} persist at all pressures with all models and buffers and may arise from a weak blended transition not included in the fit. The dispersive Voigt (dV) profile shows systematic residuals of ~2% for Ar and is generally a poor fit. For the dR fit, the β_m are floated individually for the ν_1 lines, and for the other lines, are fixed to the value determined from the previous monofit to this trace [2]. The soft-collision dispersive Galatry,

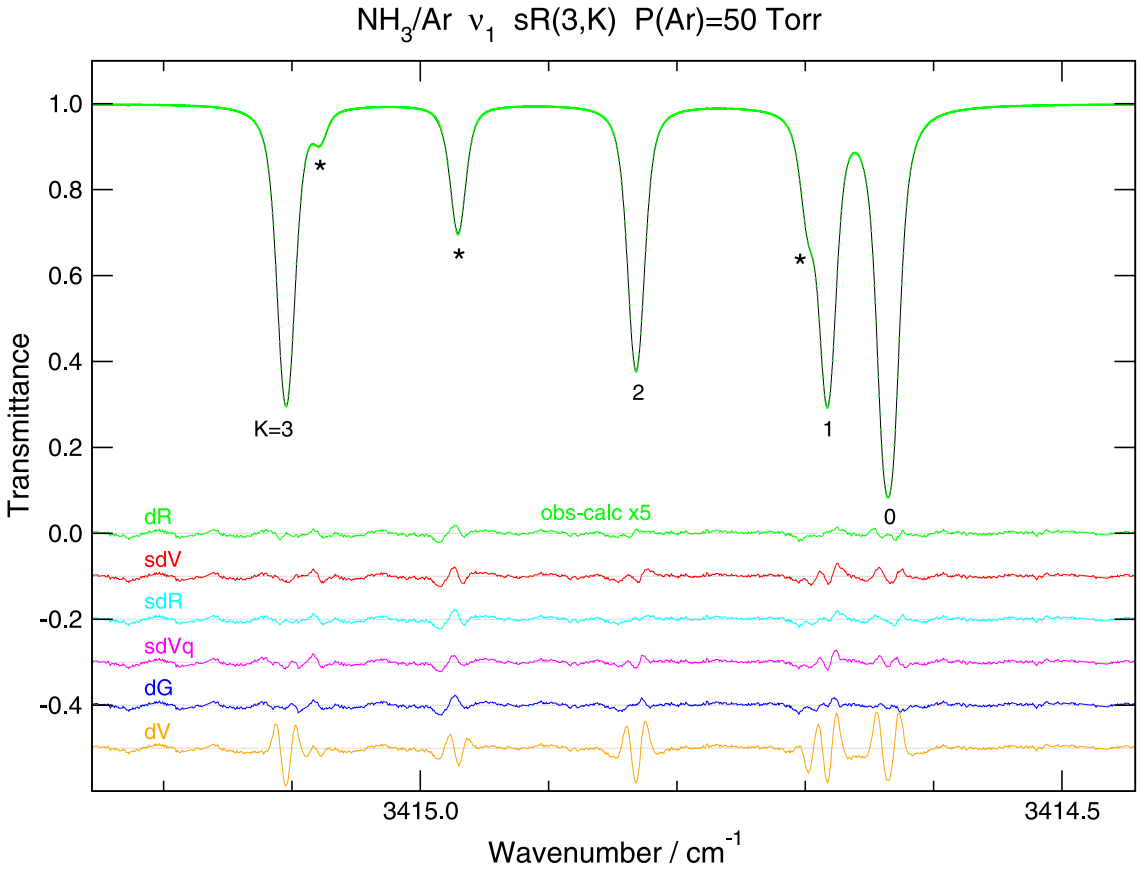

Fig. 1. Model dependence of multifit in ν_1 $sqR(3,K)$ region of NH_3 with $P(Ar) = 50$ Torr. Calculation for dR model (dotted curve). Observed–calculated residuals multiplied by 5 and offset for visibility. Model code: R, Rautian; V, Voigt; G, Galatry; d, dispersive; s, speed-dependent broadening; and q, quadratic speed-dependent broadening. K as labeled, asterisks indicate ν_3 band lines.

dG, fit is comparable to the hard-collision dR. However, we obtain almost as good a fit if we ignore Dicke narrowing altogether for the speed-dependent Voigt profiles, sdV or sdVq, using either the Berman–Ward R^{-q} model, Eq. (9), or quadratic model, Eq. (10), respectively. The fits are not significantly improved for the sdR profile which combines Dicke narrowing and speed-dependent broadening (R^{-q} model shown). Here we have constrained the β_m to be equal for all lines since they are greatly suppressed and would be negative for some lines if floated individually. This constraint contributes slightly worse residuals for sdR compared to dR in Fig. 1. However, we note that the overall multifit residuals for the sdR are improved over the dR because the speed-dependent effects dominate at higher pressures.

The deviations from the dV profile are greatest at pressures where the broadenings are comparable to the Doppler width. At much higher pressures, the dV and dR profiles are indistinguishable from each other or from a dispersive Lorentzian, dL, with an appropriate adjustment of the broadening parameter. However, neither a dL nor a speed-dependent dispersive Lorentzian, sdL (Eq. (5) with $\beta_m = 0$ and $\mathbf{k}\cdot\mathbf{v} = 0$) [27], converge for the multifits because they fail to describe the lower pressure traces. We note that the deviations from the dV profile are also $\gtrsim$1% for the N_2, O_2 and He buffers and somewhat smaller (but still observable) for self-broadening, due to masking from the larger γ_m, and for the H_2 buffer, due to the small mass ratio, $\varrho = M_b/M_a$. For self-broadening of the ν_1 Q branch, deviations from the dispersive Voigt profile are not very apparent. The unique case of He-broadened NH_3 for the $sR(3,K)$ region is shown in Fig. 2. There the dR is substantially better than the sdV profile with the R^{-q} model. This sdV fit is non-convergent as q increases without limit as $p \to 1$ (plot shown for $q = 1000$), which may reflect the weak attraction and the hard repulsive wall of the NH_3–He potential. However, the quadratic sdVq model, which is not constrained by any realistic interaction, fits better for He. The soft-collision dispersive Galatry profile [4,18] fits the He-broadened traces slightly better than the hard-collision dispersive Rautian, dR, shown.

In Table 1, we show the model dependence of the Dicke-narrowing coefficients, β, for the $sqR(3,0)$ transition for the buffer gases studied. The first row gives the β_d values predicted from Eq. (1), using the measured mass diffusion constants tabulated in [2]. The second and third rows compare the hard-collision Rautian and soft-collision Galatry values found for the previous monofits [2] to the 50 (20 for NH_3) Torr traces, ignoring

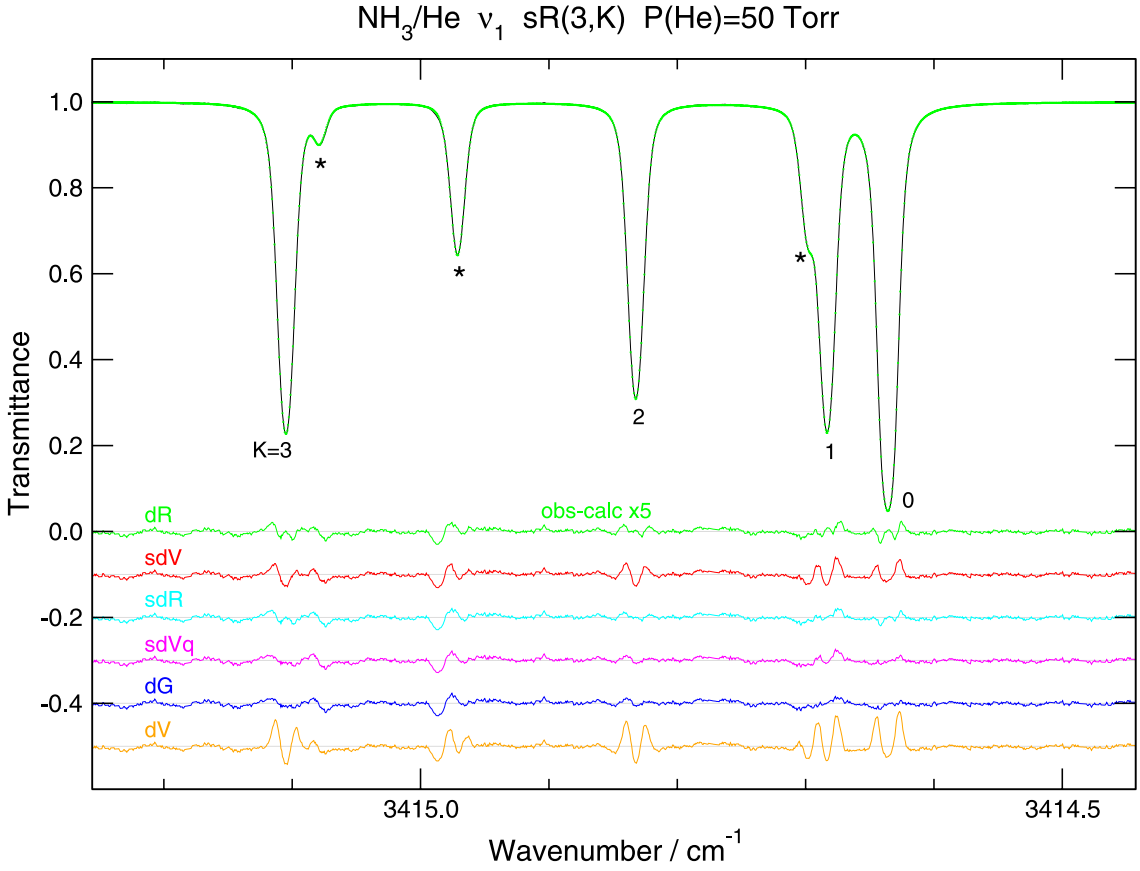

Fig. 2. Model dependence of multifit in ν_1 $sqR(3,K)$ region with $P(\mathrm{He}) = 50$ Torr. Code as in Fig. 1.

Table 1
Lineshape model dependence of Dicke-narrowing coefficients, β, in cm^{-1}/MPa for $sqR(3,0)$ line in ν_1 of NH_3 in various buffer gases

Model	N_2	O_2	H_2	Ar	He	NH_3
β_d(diff)[a]	0.3442(16)	0.3336(15)	0.0987(4)	0.3694(?)	0.1021(?)	0.4050(22)
β(R)[b]	0.3278(24)[h]	0.1705(13)	0.0545(15)	0.2009(10)	0.0737(6)	0.4292(96)
β(G)[c]	0.4065(28)	0.2402(17)	0.0747(19)	0.2892(15)	0.1193(9)	0.5254(113)
β(dR)[d]	0.3069(21)	0.1885(11)	0.0577(13)	0.2109(9)	0.0892(5)	0.3662(92)
β(dR)[e]	0.2992(40)	0.1993(23)	0.0746(24)	0.2190(21)	0.0921(13)	0.4992(139)
β(sdR)[f]	−0.0311(32)	0.0309(26)	0.0350(13)	0.1036(26)	0.0415(5)	0.6553(261)
β(dG)[g]	0.3765(50)	0.2415(28)	0.0862(30)	0.2626(25)	0.1066(15)	0.6290(169)

[a] Diffusion value: $\beta_d = k_B T/2\pi c M_a D_{ab} P$, from mass diffusion constants, D_{ab}, listed in [2].
[b] Ref. [2] Rautian monofit: β_m constrained to be equal for all lines in $R(3,K)$ 50 (20 for NH_3)Torr traces.
[c] Ref. [2] Galatry monofit: β_m constrained.
[d] Present dispersive Rautian multifit: β_m constrained.
[e] Present dispersive Rautian multifit: β_m floated.
[f] Present speed-dependent dispersive Rautian multifit: β_m constrained.
[g] Present dispersive Galatry multifit: β_m floated.
[h] Uncertainties in parentheses are one standard deviation of fit in terms of last digits.

Table 2
Transition dependence of Dicke-narrowing coefficients, β_m, in cm^{-1}/MPa for $R(J,K)$ lines in ν_1 of NH_3 in various buffer gases for dispersive Rautian fit

	N_2	O_2	H_2	Ar	He	NH_3
$aqR(0,0)$	0.3803(113)	0.2220(55)	0.0294(74)	0.2164(54)	0.1014(32)	0.8868(230)
$sqR(1,1)$	0.3366(103)	0.2069(48)	0.0610(70)	0.2153(37)	0.1013(22)	0.2443(404)
$sqR(1,0)$	0.3722(52)	0.1882(29)	0.0451(35)	0.2162(24)	0.0850(15)	0.7560(97)
$aqR(1,1)$	0.3776(99)	0.1865(45)	0.0330(63)	0.1883(34)	0.0809(20)	0.3667(375)
$sqR(3,3)$	0.3159(58)	0.1873(29)	0.0454(37)	0.2042(25)	0.0831(15)	0.1610(424)
$sqR(3,2)$	0.3221(61)	0.1849(30)	0.0668(38)	0.2210(26)	0.0872(15)	0.3114(347)
$sqR(3,1)$	0.2754(63)	0.2013(33)	0.0668(38)	0.2215(30)	0.0959(17)	0.3557(270)
$sqR(3,0)$	0.2992(40)	0.1993(23)	0.0746(24)	0.2190(21)	0.0921(13)	0.4992(139)
$aqR(3,3)$	0.3453(58)	0.1976(28)	0.0590(36)	0.2111(24)	0.0908(14)	0.2151(428)
$aqR(3,2)$	0.2434(58)	0.1551(29)	0.0139(35)	0.1851(25)	0.0672(14)	0.0251(333)
$aqR(3,1)$	0.2927(58)	0.1723(27)	0.0526(33)	0.2067(24)	0.0805(13)	0.2809(226)

line mixing and constraining all β_m in the manifold to be equal. Typically, $\beta(G) > \beta(R)$ since more soft collisions than hard are required to effect the same narrowing. The remaining entries are from the present multifits and include line mixing, which does not have a profound effect upon β. The fourth and fifth rows give the dR fitted values with constrained and freely floated β_m, respectively. These values scale roughly with the β_d for the various buffers and show some minor non-systematic model variation. As mentioned above for Eq. (8), we can attribute any $\beta_m \leqslant \beta_d$ to correlation between velocity-changing and dephasing collisions [3]. Here, only the self-collisions yield $\beta_m > \beta_d$, which is normally a signal of speed-dependent broadening [8,11,25]. When speed-dependent broadening is included for the sdR profile, the Dicke-narrowing coefficients show a drastic reduction for the foreign-gas cases, but an unusual increase for self-collisions. We believe that this is not necessarily a real physical phenomenon, but may reflect an uncertainty among highly correlated parameters in the fit. In fact, we expect very little speed dependence for NH_3 self-collisions because $q \to 3$ and $p \to 0$ for the dominant dipole–dipole interactions. The last line gives the β_m from the dG multifits, which should be more appropriate for the lighter buffers where they are seen to be closer to the β_d predictions.

When we allow the β_m for each ν_1 R-branch transition to float in the dR model, we obtain the values given in Table 2 for the various buffers. There is reasonably good consistency among all the lines with the exception of $aqR(3,2)$, which is systematically lower for all buffers. It seems unlikely that this one line has significantly more correlation than the others; but it may indicate that there is another unassigned weak line buried under it. Similarly, the large β_m for $aqR(0,0)$ for self-collisions may reflect its strong blend with the ν_3 $apP(7,7)$ line.

For the speed-dependent broadening model profiles, we give the fitted q or $\tilde{q}$ parameters in Table 3 for the various buffers for each spectral range scanned. In principle, q should be transition dependent, but we constrain it to be the same for all lines within a fitted segment for computational convenience. The simple R^{-q} potential model [9,10] would suggest $q \sim 4$ for dipole–quadrupole interactions between NH_3 and the homopolar diatomics, N_2, O_2, and H_2 and $q \sim 6$ for dipole-induced-dipole for the polarizable Ar buffer. As stated above, we expect $q \sim 3$ for the long-range dipole–dipole self-collisions and $q \gg 3$ for the rigid repulsive wall for NH_3–

Table 3
Lineshape model and R- and Q-branch manifold dependence of speed-dependent broadening parameters for ν_1 of NH_3 in various buffer gases

	N_2	O_2	H_2	Ar	He	NH_3
q(sdV)[a]						
$R(3,K)$	5.025(21)[d]	4.768(16)	15.58(1.93)	5.410(21)	1000.0(0)	3.407(14)
$R(1,K)$	5.670(49)	4.760(28)	7.48(71)	5.276(32)	1000.0(0)	4.730(38)
$R(0,K)$	5.367(74)	5.445(59)	7.28(1.10)	6.200(71)	1000.0(0)	5.311(81)
$Q(J,K)$	4.802(18)	4.961(16)	14.59(1.70)	5.395(19)	1000.0(0)	3.406(12)
q(sdR)[b]						
$R(3,K)$	5.302(38)	4.209(28)	4.0(0)	3.925(31)	1000.0(0)	2.709(21)
$R(1,K)$	5.741(69)	4.585(57)	4.04(69)	4.230(51)	1000.0(0)	2.436(14)
$R(0,K)$	5.398(112)	4.877(103)	4.0(0)	4.751(92)	1000.0(0)	5.651(122)
$Q(J,K)$	4.458(31)	4.221(29)	4.0(0)	3.724(23)	1000.0(0)	3.435(37)
$\tilde{q}$(sdVq)[c]						
$R(3,K)$	0.1214(6)	0.1222(6)	0.0308(7)	0.1610(6)	0.1153(6)	0.0318(9)
$R(1,K)$	0.1367(11)	0.1177(10)	0.0239(12)	0.1506(10)	0.1081(10)	0.0853(10)
$R(0,K)$	0.1309(18)	0.1451(15)	0.0226(20)	0.1796(14)	0.1342(15)	0.0941(17)
$Q(J,K)$	0.1135(6)	0.1282(5)	0.0295(7)	0.1613(5)	0.1261(6)	0.0311(7)

[a] Speed-dependent dispersive Voigt fit: $V(R) \sim 1/R^q$ model.
[b] Speed-dependent dispersive Rautian fit: $V(R) \sim 1/R^q$ model.
[c] Speed-dependent dispersive Voigt fit: $\gamma(v)/\langle\gamma\rangle = 1 + \tilde{q}[(v^2/\bar{v}^2) - 3/2]$ model.
[d] Uncertainties in parentheses are one standard deviation in terms of last digits. (0) = fixed.

He. The fitted values given in Table 3 for the sdV model are in rough accord with these predictions except for the light buffers, He and H_2. As noted above, we fixed $q = 1000$ for the He buffer since it does not converge to a finite value, whereas H_2 converges to a high value, possibly indicative of repulsive effects. For the sdR model, the q values generally decrease from the sdV model since Dicke narrowing accounts for some of the non-Voigt character. For H_2, the sdR does not always converge; so we fix $q = 4$ for the dipole–quadrupole

Table 4
Lineshape model dependence of spectral parameters for self-broadening of the $sqQ(3,3)$ and $sqR(3,0)$ transitions in the ν_1 band of NH_3

Line Model	ω_m (cm^{-1})	S_m (cm^{-2}/MPa)	δ_m (cm^{-1}/MPa)	γ_m (cm^{-1}/MPa)	β_m (cm^{-1}/MPa)	ζ_m (1/MPa)
$sqQ(3,3)$						
dR[a]	3336.390404(3)[g]	5.3657(16)	0.0423(28)	6.4395(20)	0.4292(0)	−3.857(45)
dR[b]	3336.390404(3)	5.3656(16)	0.0423(28)	6.4393(20)	0.420(10)	−3.856(45)
dR[c]	3336.390403(3)	5.3665(16)	0.0431(28)	6.4411(21)	0.503(36)	−3.874(45)
dV[d]	3336.390404(3)	5.3620(16)	0.0427(28)	6.4312(20)	0.0(0)	−3.852(46)
sdV[d,e]	3336.390403(3)	5.3681(16)	0.0423(28)	6.4484(21)	0.0(0)	−3.857(45)
sdR[b,e]	3336.390403(3)	5.3683(16)	0.0423(28)	6.4493(24)	−0.028(33)	−3.857(45)
sdVq[d,f]	3336.390403(3)	5.3682(16)	0.0417(28)	6.4500(21)	0.0(0)	−3.848(45)
R[c]	3336.390465(4)	5.3371(22)	−0.1600(20)	6.4263(29)	0.527(51)	0.0000(0)
$sqR(3,0)$						
dR[a]	3414.636261(3)	4.1817(11)	0.0273(21)	3.0636(15)	0.4292(0)	0.008(75)
dR[b]	3414.636261(3)	4.1806(11)	0.0277(21)	3.0615(15)	0.3662(92)	−0.050(76)
dR[c]	3414.636264(3)	4.1835(11)	0.0260(21)	3.0630(16)	0.499(14)	0.050(76)
dG[c]	3414.636263(3)	4.1841(12)	0.0251(21)	3.0706(16)	0.629(17)	0.133(76)
dV[d]	3414.636261(3)	4.1743(11)	0.0301(21)	3.0499(15)	0.0000(0)	−0.387(78)
sdV[d,e]	3414.636262(3)	4.1790(11)	0.0266(21)	3.0610(16)	0.0000(0)	−0.071(76)
sdR[b,e]	3414.636261(3)	4.1826(11)	0.0278(21)	3.0643(16)	0.655(26)	−0.064(75)
sdVq[d,f]	3414.636262(3)	4.1793(11)	0.0260(21)	3.0626(16)	0.0000(0)	−0.039(76)
R[c]	3414.636293(4)	4.2041(18)	−0.0007(22)	3.1193(26)	0.727(25)	0.0000(0)

[a] β_m fixed.
[b] β_m constrained.
[c] β_m floated.
[d] $\beta_m = 0$.
[e] Speed dependence model: $V(R) \sim 1/R^q$.
[f] Speed dependence model: $\gamma(v)/\langle\gamma\rangle = 1 + \tilde{q}[(v^2/\bar{v}^2) - 3/2]$.
[g] Uncertainties in parentheses are one standard deviation in terms of last digits. (0)=fixed.

attraction. The sdR produces an increase of q for the N_2 buffer in the $R(3,K)$ region, where β_m becomes unphysically negative as seen in Table 1. Another curious result is for the sdR model with self-collisions where $q < 3$ for the $R(3,K)$ and $R(1,K)$ manifolds. Such long-range potentials are not physically meaningful for neutral molecules, but this result implies a negative speed dependence to the broadening and accounts for the increase of β_m for sdR over dR for NH_3 seen in Table 1. Again, because the q and β_m parameters are so strongly correlated in the fits, it is not possible to reliably interpret these results physically. We also have no physical rationale for the $\widetilde{q}$ parameters for the quadratic speed dependence sdVq model, Eq. (9); noting that most are $\widetilde{q} \sim 0.1$ (as found previously for CO [8,11]) except for lower values for H_2 and NH_3 which show smaller Voigt deviations.

Another consequence of the R^{-q} potential model is that it predicts $\gamma \propto T^{-\kappa}$ with $\kappa = 1-(q-3)/2(q-1)$. Here, we have recorded only room temperature spectra, but Nemtchinov et al. [15] recently measured a set of N_2-, O_2- and H_2-broadened P- and R-branch lines in the ν_2 band of NH_3 for $200 \leqslant T \leqslant 296$ K. They obtained a wide range of temperature exponents, $0.48 \leqslant \kappa \leqslant 0.94$ for N_2, $0.65 \leqslant \kappa \leqslant 0.97$ for O_2, and $0.32 \leqslant \kappa \leqslant 0.95$ for H_2, with the highest values for rotations about the figure axis, $K \sim J$. The expected $q = 4$ for these buffers predicts $\kappa \sim 0.83$ independent of rotation.

The effect of the different lineshape models on the other spectroscopic and collision parameters is examined in Table 4 for self-broadening of the strong $sqQ(3,3)$ and $sqR(3,0)$ transitions. For the dispersive profiles, the transition wavenumbers, ω_m, intensities, S_m, shifts, δ_m, broadenings, γ_m, and line-mixing coefficients, ζ_m, generally agree within the 1σ least-squares uncertainties. Somewhat larger discrepancies are obtained for the S_m, γ_m, and ζ_m for the poorly fitting dV profile. Note that the ζ_m for the $sqR(3,0)$ line is so small, it is indeterminate. If line mixing is ignored, as for the non-dispersive Rautian, all the parameters, particularly the shifts, readjust to compensate. As discussed above, the narrowing coefficients, β_m, strongly depend on the model and must be considered "effective" parameters.

6. Line mixing and collisional propensities

The effects of line mixing are most apparent at the higher pressures measured. In Fig. 3, we show the 200 Torr trace of Ar-broadened NH_3 for the ν_1 $R(3,K)$ manifold

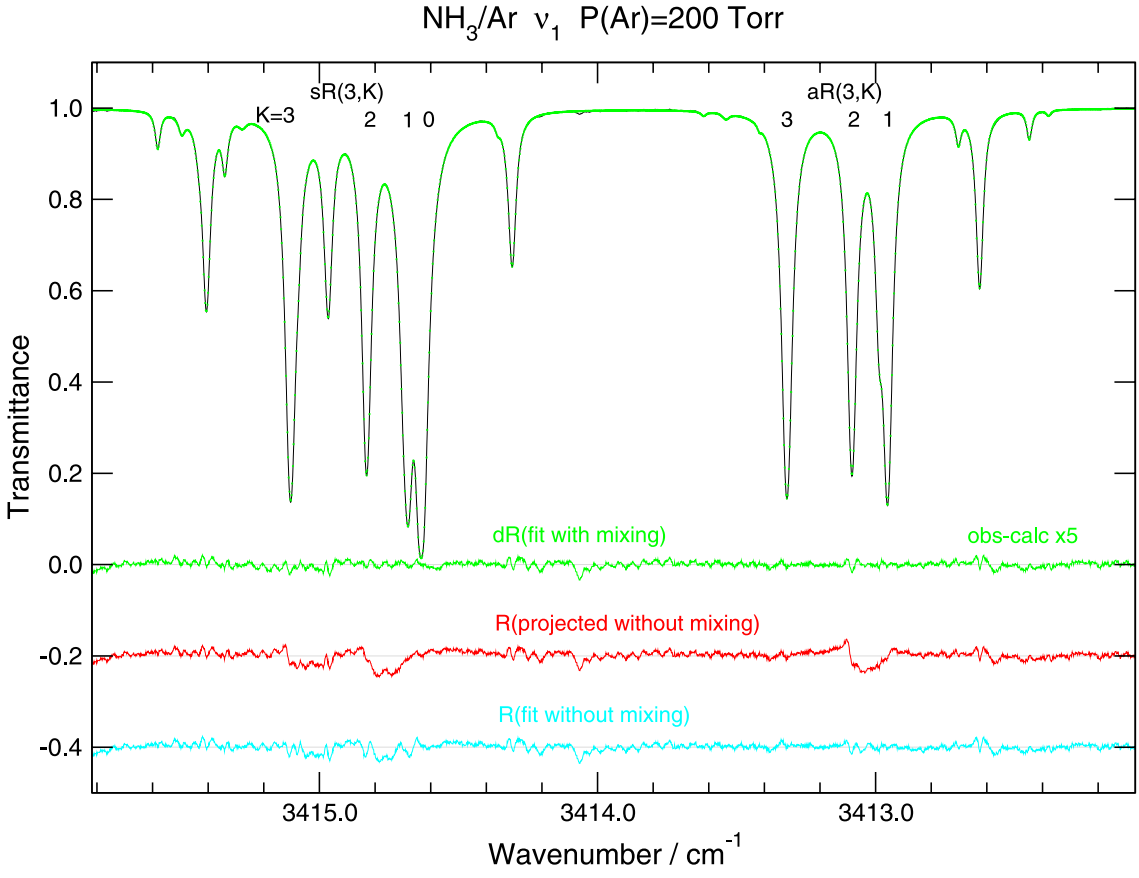

Fig. 3. Line mixing in $qR(3,K)$ manifold of ν_1 band of NH_3 with $P(\mathrm{Ar}) = 200$ Torr. Code as in Fig. 1.

multifitted to the dispersive Rautian profile. The residuals from the Rautian projected without mixing are obtained by simply recalculating the spectrum with $\zeta_m = 0$. Here the deviations represent the contribution of line mixing to the multifit. If we refit the dispersionless Rautian to the spectra, the parameters (primarily the shifts) readjust to minimize the residuals, shown by the bottom trace, with a consequent deterioration of the fit at lower pressures. The largest deviations for the projected Rautian case occur between the $K = 1$ and $K = 2$ lines for both the symmetric and antisymmetric tunneling levels. The threefold pyramidal axis of NH_3 precludes collisional coupling between $K = 0 \bmod 3$ and $K = 1 \bmod 3$ or $K = 2 \bmod 3$ levels. For the $sqR(3,K)$ transitions, there is also some observable contribution due to coupling between $K = 0$ and $K = 3$. Spin statistics eliminate the $aqR(3,0)$ line, so there is no comparable mixing for the $aqR(3,3)$ line. We see little evident collisional coupling between tunneling levels for ν_1, or for the more closely spaced ν_3 tunneling partners. Note that the $s - a$ tunneling splittings for the ν_1 band are the sum ($\sim 1.8\,cm^{-1}$), and for ν_3 the difference ($\sim 0.4\,cm^{-1}$), of the tunneling splittings in the ground and excited vibrations.

Dhib et al. [28] have discussed the collisional selection rules for NH_3 arising from various components of the intermolecular potential. For $\Delta J = 0$ collisions, either $s \leftrightarrow a$ with $\Delta K = 0$ or $s \to s, a \to a$ with $\Delta K = \pm 3$. The observed couplings within the $R(3,K)$ manifold between $K = 1$ and 2 arise from $\Delta K = \pm 3$ transfer, since each K level is composed of a degenerate $\pm K$ pair. In Fig. 4, we show the line-mixing contributions from the deviations in the residuals from the projected Rautian within $R(3,K)$ for each of the perturbers studied here. Only the observed He-broadened spectrum is shown for orientation. There is a progression from the $\Delta K = \pm 3$ to the $s \leftrightarrow a$ coupling as the broadening increases from He to NH_3. Self-broadening is dominated by $s \leftrightarrow a$ coupling, which is particularly evident for the closer ν_3 band pairs, but is still observable between more remote ν_1 partners. Note that there is no tunneling counterpart for $sqR(3,0)$, which explains the small ζ_m for this line given in Table 4. Rotational coupling between the K lines is also evident for self-broadening, but it plays a secondary role. The line-mixing patterns observed for the quadrupolar perturbers, O_2, N_2, and H_2, exhibit both $\Delta K = \pm 3$ and $s \leftrightarrow a$ couplings. There is also some observable $s \leftrightarrow a$ coupling for Ar for the $\nu_3\, pP(7,7)$ tunneling doublet bracketing the $\nu_1\, qR(0,0)$ line. Line mixing between the various J manifolds in the P and R branches is negligible at these pressures because of their large separation, $\gtrsim 20\,cm^{-1}$.

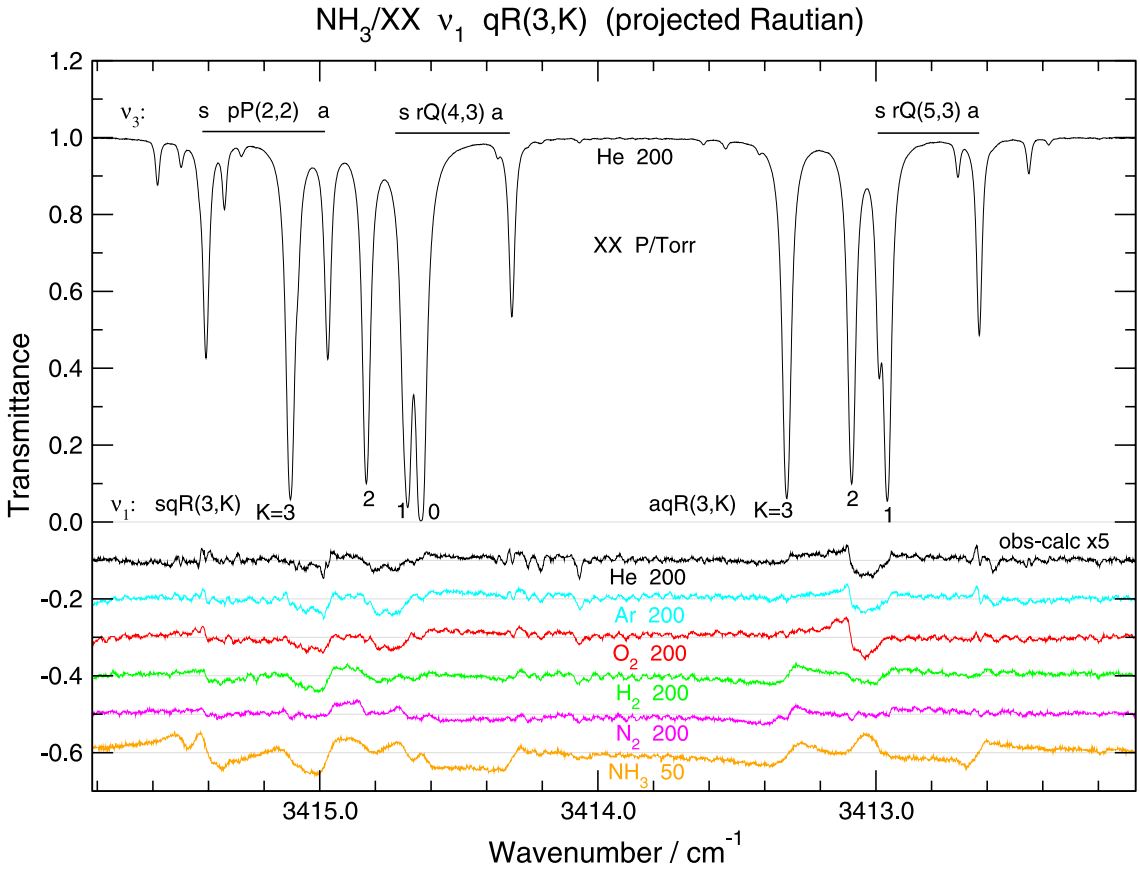

Fig. 4. Line mixing in $qR(3,K)$ manifold of ν_1 band of NH_3 with different perturbers. Residuals 5× from Rautian projected without mixing.

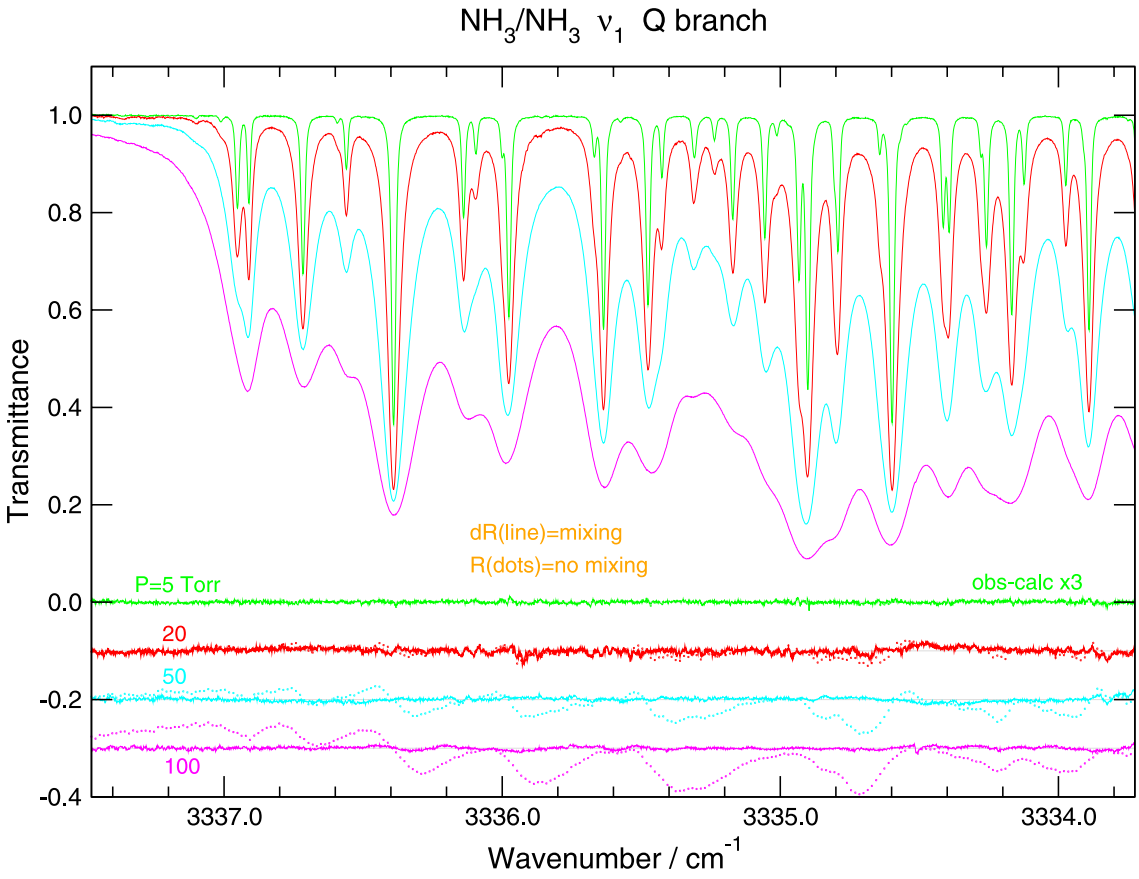

Fig. 5. Line mixing in ν_1 $qQ(J,K)$ branch with $P(NH_3) = 5$, 20, 50, and 100 Torr. Residuals 3×. Dispersive Rautian model solid line; projected Rautian dotted line.

For the self-broadened Q branch, the close proximity of transitions with different J allows many other couplings [28]. Thus, the line-mixing pattern is more complicated as shown in Fig. 5, but the tunneling couplings still dominate. Here, the residuals are multiplied by 3 and are given by solid lines for the dispersive Rautian profile and by dotted lines for the projected Rautian calculations without line mixing. Line mixing becomes observable at pressures as low as 20 Torr for self-broadening and is essential to the multifit at higher pressure. The sharp structure observable at 20 Torr near 3335.9 cm^{-1} arises from weak lines not included in the fits.

We note that there have been several studies of line mixing between NH_3 inversion doublets in the ground state [29], ν_3 [30], and ν_4 [31–33]. In the case of self-broadening, the coupling is strong and unambiguous [30,33]. However, for non-polar buffer gases, the effect is generally weaker [29,31–33]. High-pressure studies of NH_3 in a variety of buffers [34] exhibit strong line mixing in the ν_1 and ν_2 Q branches and even between J manifolds in the P and R branches, and demonstrate the need to use a full relaxation matrix inversion procedure to adequately describe the absorption contours.

7. An anomaly

In Fig. 6, we show the pressure dependence of the self-broadened spectra of the $R(3,K)$ manifold fit to the dispersive Rautian lineshape. The fits are excellent and almost within the experimental noise throughout, with the exception of the anomalous feature at 3415.47 cm^{-1} seen in the highest two pressure scans. This anomaly is not observable in the lower-pressure self-broadened scans or at any pressure for the foreign-gas buffers. Since it occurs twice, it is probably not an instrumental artifact. Its wavenumber does not correspond to any likely impurity, its intensity grows faster than linear in pressure, it is narrower than any individual NH_3 line, and there is no other such feature in the regions we have scanned. It is tempting to invoke a molecular complex or collision-induced feature, but it is difficult to imagine such a simple spectrum for NH_3. At present, we have no explanation for this feature, but believe it is worthy of further study.

8. Results

Even with the present signal-to-noise ratio ($\gtrsim$1000), we cannot reliably distinguish the combined contribu-

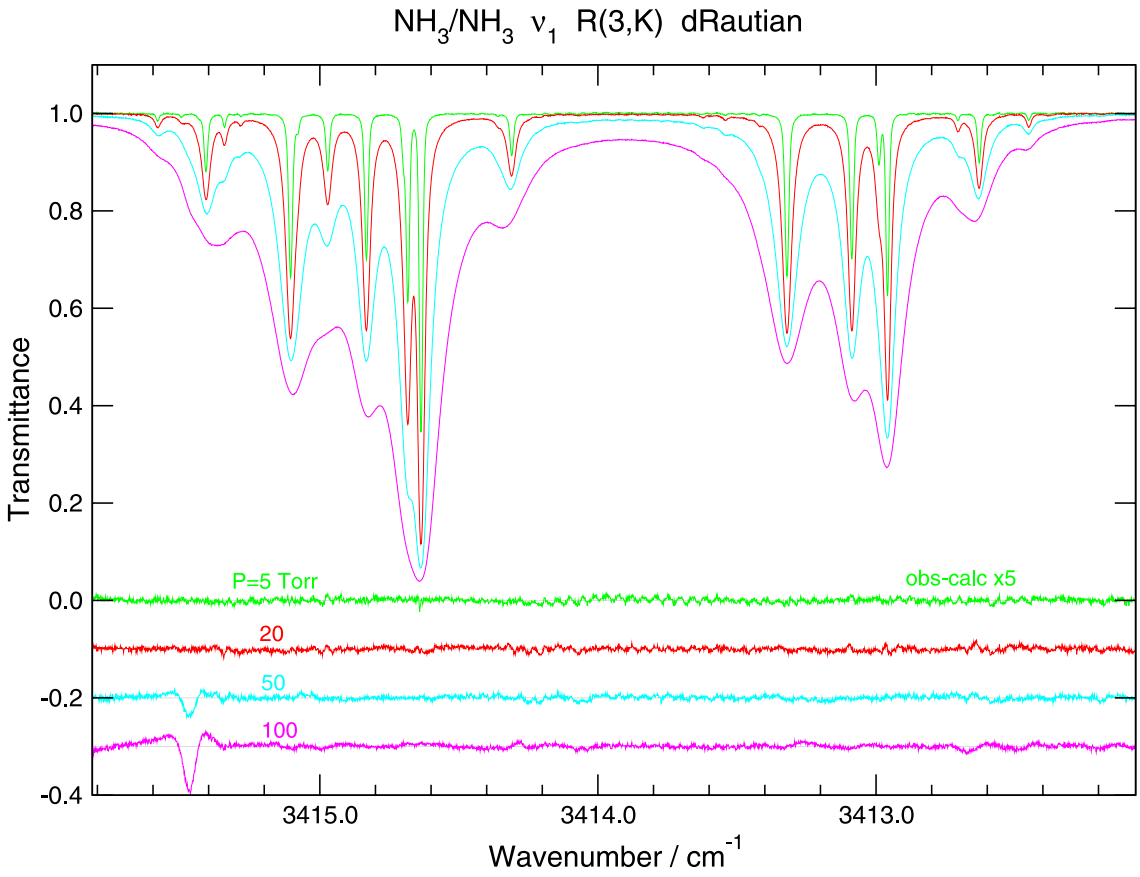

Fig. 6. Self-broadening in ν_1 $qR(3,K)$ manifold with $P(NH_3) = 5$, 20, 50, and 100 Torr multifit to dR model showing anomalous feature at 3415.47 cm^{-1}. Residuals 5×.

tions of Dicke narrowing and speed-dependent broadening to the sdR lineshapes over the measured pressure range. Convincing arguments could be made for either mechanism alone, since both the dR and sdV models fit the data reasonably well, and since the Dicke-narrowing coefficients, β_m, from the dR profile scale with the diffusion predictions for the various buffers, and the sdV speed-dependent broadening parameters, q, are consistent with those expected from the multipolar interactions. Such an ambiguity has also been obtained for methane lineshapes [6,7]. Other molecular systems have yielded more definitive mechanisms. For example, there is a clear preference for speed-dependent broadening in CO [8,11,27], whereas Dicke narrowing dominates for HF/Ar [24] where the speed dependence is known from quantum close-coupling calculations [23]. For the present data set, we see no particular advantage for the speed-dependent profiles over the standard Dicke-narrowing models. In addition, the conventional hard-collision Dicke-narrowing model, Eq. (7), is computationally ~5 times faster than the speed-dependent profiles and nearly as fast as the Voigt. Therefore, we restrict the rest of our discussion to the results from the dR fits.

The spectroscopic parameters for the self-broadened $R(0)$, $R(1)$, and $R(3)$ manifolds and Q branch obtained for the dR multifits are tabulated in Appendix A. A comparison with the monofit analysis [1] shows that we include and assign [13,14] several more lines, that the S_m, δ_m, and γ_m parameter uncertainties are considerably smaller and fewer of them are constrained or fixed, and that the individual Dicke-narrowing and line-mixing coefficients can be determined. The self shifts are one to two orders of magnitude smaller than the self-broadenings, and, where determinable, their signs depend on the inversion symmetry. Inclusion of line mixing in first order permits us to extend the fits to higher pressure, but a full relaxation matrix inversion [6,7,19,34] may be required at even higher pressure. The opposite signs and nearly equal magnitudes of the ζ_m for the ν_1 and ν_3 $s-a$ tunneling partners are another indication of the dominant coupling for self-broadening. The significant ζ_m for the ν_1 $aqR(0,0)$ line, which has no nearby lines to which it can couple, may be a fitting artifact due to the blended ν_3 $apP(7,7)$ line. The intensities and broadening coefficients generally agree within 1 or 2% with the previous analysis [1] for the stronger isolated lines. The weak lines, however, are more strongly influenced by baseline uncertainties and show larger discrepancies. A few lines with fixed parameters outside the scanned regions are included if their high-pressure wings affect the

baseline. The uncertainties given in the tables are just 1σ least-squares fitting errors and do not reflect any systematic calibration, model or baseline errors or the influence of unresolved blended lines. The transition wavenumbers, though recalibrated against HITRAN2K [13,14], should be more precise here, since we are able to curve resolve many of the multiple-assignment blends in HITRAN2K. For the foreign-gas broadeners, the shifts are generally negative except for He, where they are mostly positive [2]. Computer readable ASCII listings for the extensive self- and foreign-gas-broadening parameters can be obtained from the first author or the journal archive. These listings contain the weak lines necessary to fit observed spectra even if they are unassigned.

9. Broadenings

In this section, we examine the systematic dependence of the broadenings on rotation, tunneling, buffer gas, and vibration. The top half of Table 5 gives our results for the v_1 band R-branch lines we have scanned. As expected, the broadenings for respective $s-a$ tunneling partners are nearly identical and yield a realistic estimate of the measurement uncertainty of $\lesssim 1\%$. For the foreign gases, there is only a weak J dependence when $K=J$, but a more moderate $J-K$ dependence; self-broadening shows stronger $J=K$ and $J-K$ effects. The buffer gas dependence is very strong and is in rough accord with the known multipole moments and polarizabilities of the species [28,35]. The small systematic decrease in foreign-gas broadenings compared with our previous report [2], are due to the self-broadening correction.

The bottom half of Table 5 compares our result with the recent FTS measurements in the v_2 band by Nemtchinov, Sung and Varanasi, NSV [15] and in the v_0 pure-rotational ground state by Brown and Peterson, BP [16]. All are parallel band ($\Delta K=0$) transitions. The agreement for foreign-gas broadenings for corresponding rotational transitions is excellent, generally within 1 or 2%, indicating little vibrational dependence. For self-broadening, the v_2 band transitions are systematically smaller than the v_1, which may reflect the much larger tunneling splittings in the excited v_2 umbrella mode [36]. Collisional tunneling transitions and resonances are less important for the non-polar buffer gases. The ground-state v_0 self-broadenings are consistent with the v_1 for $R(3,K)$, but are scattered at lower J where the FTS spectrum was very noisy [16]. Both NSV and BP fit their R- and P-branch broadenings to a polynomial in J and K in order to provide an empirical interpolation and extrapolation scheme for all transitions. These simple expansions were satisfactory for the non-polar buffers, but fit poorly for self-broadening at low J [15,16]. Insofar as our v_1 R-branch broadenings are

Table 5
J, K, parity, and vibrational dependence of NH_3 R-branch broadening coefficients, γ_m, in cm^{-1}/MPa for various buffer gases

Line	$N_2(v_1)$[a]	$O_2(v_1)$	$H_2(v_1)$	$Ar(v_1)$	$He(v_1)$	$NH_3(v_1)$
$aqR(0,0)$	1.1197(9)	0.6258(6)	0.9414(8)	0.4603(11)	0.3295(7)	3.3823(19)
$sqR(1,0)$	1.0502(4)	0.5990(3)	0.8563(4)	0.4747(3)	0.2978(2)	2.6065(9)
$sqR(1,1)$	1.1167(8)	0.6462(5)	0.9515(7)	0.5123(4)	0.3398(3)	5.1783(42)
$aqR(1,1)$	1.1157(6)	0.6406(4)	0.9420(5)	0.5064(3)	0.3359(3)	5.1817(22)
$sqR(3,0)$	0.9570(4)	0.5439(3)	0.7064(3)	0.4504(3)	0.2648(2)	3.0630(16)
$sqR(3,1)$	0.9842(8)	0.5596(5)	0.7468(6)	0.4535(5)	0.2760(4)	3.7606(40)
$aqR(3,1)$	0.9829(6)	0.5542(3)	0.7433(4)	0.4488(3)	0.2748(2)	3.7425(23)
$sqR(3,2)$	1.0407(4)	0.5904(3)	0.8334(3)	0.4716(3)	0.3001(2)	4.9355(26)
$aqR(3,2)$	1.0386(4)	0.5926(3)	0.8343(3)	0.4730(3)	0.3024(2)	4.9426(25)
$sqR(3,3)$	1.0861(4)	0.6066(3)	0.8801(4)	0.4867(3)	0.3055(2)	6.1386(28)
$aqR(3,3)$	1.0977(4)	0.6077(3)	0.8857(3)	0.4863(3)	0.3060(2)	6.2098(25)
	$N_2(v_2)$[b]	$O_2(v_2)$	$H_2(v_2)$	$NH_3(v_2)$	$H_2(v_0)$[c]	$NH_3(v_0)$
$aqR(0,0)$	1.118	0.634	0.963	3.168		
$sqR(1,0)$					0.857	2.37
$sqR(1,1)$					0.962	5.75
$aqR(1,1)$	1.104	0.658	0.949	5.025	0.931	3.56
$sqR(3,0)$					0.693	3.42
$sqR(3,1)$					0.743	3.81
$aqR(3,1)$	0.995	0.566	0.757	3.286	0.712	3.88
$sqR(3,2)$					0.844	5.12
$aqR(3,2)$	1.054	0.599	0.853	4.277	0.788	5.07
$sqR(3,3)$					0.876	6.23
$aqR(3,3)$	1.102	0.627	0.905	5.590	0.893	6.42

[a] v_1 band measurements, present work.
[b] v_2 band measurements from NSV, Ref. [15]; errors ~3%.
[c] v_0 ground-state measurements from BP, Ref. [16]; errors ~2% for H_2, ~8% for NH_3.

Table 6
NH_3 ν_1 band Q-branch broadening coefficients, γ_m, in cm^{-1}/MPa at $T = 296$ K in various buffer gases using the dispersive Rautian model

Line	ω_m	N_2	O_2	H_2	Ar	He	NH_3
sqQ(1,1)	3336.95174	1.1293(8)	0.6382(5)	0.9474(8)	0.4921(4)	0.3377(4)	5.8831(60)
sqQ(2,2)	3336.71603	1.0948(5)	0.6241(4)	0.8949(5)	0.5013(3)	0.3110(3)	6.3318(31)
sqQ(2,1)	3336.56023	1.0343(14)	0.6254(8)	0.8934(13)	0.5069(6)	0.3174(5)	3.8962(70)
sqQ(3,3)	3336.39040	1.0638(5)	0.5870(3)	0.8419(4)	0.4734(2)	0.2831(2)	6.4411(21)
sqQ(3,2)	3336.13898	1.0287(10)	0.6057(4)	0.8714(9)	0.4877(4)	0.3096(5)	4.9486(47)
sqQ(3,1)	3336.00079	1.0246(33)	0.6089(17)	0.8190(28)	0.5030(13)	0.3013(9)	3.542(13)
sqQ(4,4)	3335.97592	1.0244(6)	0.5706(4)	0.8081(5)	0.4756(4)	0.2705(3)	6.4642(36)
sqQ(4,3)	3335.63580	1.0098(5)	0.5746(4)	0.8410(5)	0.4642(3)	0.2944(3)	5.4518(31)
sqQ(5,5)	3335.47565	0.9720(5)	0.5400(4)	0.7595(5)	0.4611(3)	0.2616(3)	6.4630(36)
sqQ(4,2)	3335.42559	0.9288(13)	0.5351(7)	0.7442(10)	0.4350(6)	0.2723(4)	4.2393(78)
sqQ(4,1)	3335.31340	0.9043(72)	0.4869(33)	0.6688(56)	0.3826(23)	0.2314(16)	3.251(31)
aqQ(1,1)	3335.17122	1.0837(7)	0.6066(5)	0.9028(7)	0.4673(4)	0.3134(4)	5.7674(54)
sqQ(5,4)	3335.05562	0.9773(7)	0.5514(4)	0.8091(6)	0.4416(4)	0.2706(3)	5.6033(51)
sqQ(9,8)	3335.01271	0.9388(37)	0.4908(15)	0.7480(29)	0.3985(11)	0.2176(7)	5.446(36)
aqQ(2,2)	3334.93296	1.0948(10)	0.6283(6)	0.9022(9)	0.5011(7)	0.3173(6)	6.415(11)
sqQ(6,6)	3334.90114	0.9316(7)	0.5125(5)	0.7265(6)	0.4416(4)	0.2402(3)	6.4535(58)
aqQ(2,1)	3334.80548	1.0538(40)	0.6389(16)	0.9138(36)	0.5231(17)	0.3266(13)	3.888(17)
sqQ(5,3)	3334.79248	0.9476(13)	0.5364(6)	0.7610(11)	0.4305(6)	0.2690(6)	4.8489(80)
sqQ(5,2)	3334.64271	0.8979(24)	0.5230(12)	0.6868(19)	0.4341(9)	0.2633(6)	3.980(16)
aqQ(3,3)	3334.59822	1.0528(6)	0.5827(4)	0.8337(5)	0.4671(3)	0.2824(2)	6.4329(29)
sqQ(5,1)	3334.56833	0.8870(115)	0.5261(59)	0.6653(90)	0.4745(48)	0.2781(28)	3.508(64)
sqQ(6,5)	3334.41433	0.9311(10)	0.5270(6)	0.7683(9)	0.4293(5)	0.2603(6)	5.6498(76)
aqQ(3,2)	3334.39313	0.9890(10)	0.5793(6)	0.8288(9)	0.4686(5)	0.3015(7)	4.8115(61)
aqQ(3,1)	3334.27949	0.9645(31)	0.5779(16)	0.7695(26)	0.4661(12)	0.2826(8)	3.451(14)
sqQ(7,7)	3334.25890	0.8938(7)	0.4965(4)	0.7101(6)	0.4285(4)	0.2346(3)	6.4029(65)
aqQ(4,4)	3334.16796	1.0046(5)	0.5732(4)	0.8001(5)	0.4750(4)	0.2757(3)	6.4338(38)
sqQ(6,4)	3334.12331	0.8843(11)	0.5062(6)	0.7318(10)	0.4053(5)	0.2479(4)	4.9758(88)
sqQ(6,3)	3333.97356	0.8382(15)	0.4887(10)	0.6615(11)	0.4051(9)	0.2395(6)	4.1761(53)
sqQ(6,2)	3333.90901	0.8464(100)	0.5079(59)	0.6450(78)	0.4482(52)	0.2612(33)	3.294(26)
aqQ(4,3)	3333.89033	0.9766(10)	0.5739(8)	0.8331(10)	0.4637(7)	0.3045(6)	5.3653(25)
aqQ(4,2)	3333.71826	0.9590(21)	0.5464(12)	0.7619(15)	0.4360(11)	0.2756(7)	4.2908(66)
aqQ(5,5)	3333.64440	0.9648(11)	0.5437(9)	0.7708(10)	0.4589(8)	0.2614(6)	6.4537(39)
aqQ(4,1)	3333.62595	0.969(12)	0.5167(61)	0.7481(99)	0.4213(50)	0.2371(30)	3.722(30)
sqQ(8,3)	3333.58927	0.693(12)	0.4527(70)	0.5472(95)	0.3966(62)	0.2401(38)	3.343(33)
sqQ(7,6)	3333.57298	0.9332(15)	0.5223(10)	0.7766(14)	0.4279(10)	0.2566(7)	5.7441(53)
sqQ(8,8)	3333.50988	0.8414(26)	0.4718(15)	0.6801(21)	0.4200(14)	0.2353(9)	6.622(13)
sqQ(7,5)	3333.49920	0.8919(49)	0.4774(23)	0.7182(37)	0.3750(18)	0.2400(15)	4.792(14)
sqQ(8,5)	3333.42110	0.7666(71)	0.4113(29)	0.5776(53)	0.3386(26)	0.2042(17)	4.378(22)
sqQ(7,4)	3333.39830	0.8234(38)	0.4690(13)	0.6295(31)	0.3777(75)	0.2052(14)	3.9188(51)
aqQ(5,4)	3333.30392	0.8872(52)	0.4812(27)	0.7019(28)	0.3886(26)	0.2735(19)	5.6148(30)
aqQ(5,3)	3333.08619	0.9269(13)	0.5333(9)	0.7521(11)	0.4370(8)	0.2710(7)	4.7347(39)
aqQ(6,6)	3333.02497	0.9310(9)	0.5006(7)	0.7241(9)	0.4379(6)	0.2518(4)	6.4110(25)
aqQ(5,2)	3332.96192	0.9902(49)	0.5465(23)	0.7421(36)	0.4626(20)	0.2722(12)	3.876(12)
sqQ(8,6)	3332.93809	0.8872(28)	0.4763(14)	0.7064(18)	0.3810(12)	0.2190(7)	5.0301(78)
aqQ(6,5)	3332.63995	0.9240(25)	0.5304(15)	0.7953(20)	0.4373(14)	0.2678(9)	5.9754(92)
aqQ(6,4)	3332.39828	0.9012(17)	0.5078(10)	0.7364(13)	0.4071(9)	0.2550(6)	4.9568(62)
aqQ(7,7)	3332.34862	0.8937(10)	0.4924(7)	0.7151(9)	0.4267(7)	0.2407(6)	6.3404(43)
aqQ(9,7)	3332.29562	0.9385(66)	0.4948(29)	0.7424(50)	0.3835(23)	0.2230(14)	5.291(32)
aqQ(6,3)	3332.27009	0.8985(28)	0.5089(14)	0.6980(17)	0.4140(12)	0.2480(7)	4.2173(57)
aqQ(6,2)	3332.21190	0.8458(63)	0.4914(30)	0.6509(46)	0.3995(24)	0.2440(16)	3.519(16)
aqQ(9,3)	3332.18984	0.792(10)	0.4746(50)	0.6155(74)	0.3901(40)	0.2120(25)	2.848(20)
aqQ(7,6)	3331.92290	0.8666(30)	0.4792(25)	0.6959(28)	0.4286(30)	0.2359(16)	6.188(16)
aqQ(9,5)	3331.82102	0.8205(90)	0.5035(53)	0.7051(79)	0.4002(42)	0.2679(31)	4.141(36)
aqQ(9,6)	3331.73864	0.8970(35)	0.4835(17)	0.7054(28)	0.3863(14)	0.2290(10)	4.777(13)
aqQ(7,5)	3331.71355	0.8863(23)	0.4990(13)	0.7334(17)	0.3995(12)	0.2367(7)	5.2387(84)
aqQ(8,8)	3331.62867	0.8669(13)	0.5028(22)	0.6997(13)	0.3999(19)	0.2485(12)	6.396(16)
aqQ(7,4)	3331.59543	0.7874(48)	0.4818(28)	0.6277(41)	0.4048(23)	0.2380(15)	3.855(14)
sqQ(9,9)	3331.46924	0.8414(10)	0.4645(7)	0.6735(9)	0.4019(7)	0.2265(6)	6.1964(45)
aqQ(8,3)	3331.35878	0.6825(43)	0.4166(26)	0.5660(37)	0.3570(23)	0.2147(16)	3.291(15)
aqQ(8,4)	3331.23942	0.838(11)	0.4472(48)	0.6590(85)	0.3478(36)	0.2019(23)	4.0305(0)
aqQ(8,7)	3331.17795	0.8895(23)	0.4839(12)	0.7271(19)	0.3999(10)	0.2283(7)	5.697(12)
aqQ(8,5)	3331.06660	0.9011(94)	0.4716(50)	0.6509(82)	0.3770(40)	0.2277(26)	4.310(28)
aqQ(8,6)	3331.03763	0.8730(17)	0.4758(10)	0.7081(13)	0.3858(9)	0.2270(6)	5.1740(56)

in agreement with theirs, these empirical models should apply.

Our ν_1 Q-branch broadenings are given in Table 6, where we have eliminated some of the weaker or blended lines which are less well determined. Here again, the results are more extensive and precise than previously reported [2] and are corrected for self-broadening, and as before, we find excellent agreement between corresponding $s-a$ tunneling partners. The rotational and buffer gas systematics in these Q-branch broadenings are shown graphically in Fig. 7 for self-broadening and Fig. 8 for foreign gases. Self-broadening of the $J=K$ transitions are remarkably constant, but decrease strongly with $J-K$. Foreign-gas broadening shows a weak steady decrease with J and $J-K$, with a somewhat larger $J-K$ dependence for N_2 and H_2. O_2 has a relatively small quadrupole moment [28] and behaves more like the rare gases.

NSV [15] did not report any ν_2 Q-branch broadenings for comparison, but we found reasonably good correspondence with ground-state tunneling microwave measurements and ν_2 Q-branch diode laser data in our earlier papers [1,2]. Since then, Fabian et al. [37] reported FTS measurements of N_2, O_2 and air broadenings in the ν_2 R and Q branches which have a weighted average ratio of $\langle\gamma_m(\nu_2)/\gamma_m(\nu_1)\rangle = 1.46(12)$ for N_2 and $\langle\gamma_m(\nu_2)/\gamma_m(\nu_1)\rangle = 1.38(13)$ for O_2 for the 40 lines corresponding to our ν_1 measurements. However, we do not believe these represent a systematic vibrational dependence since there are similar discrepancies between [37] and the more accurate recent ν_2 measurements in [15]. Moreover, Fabian et al. later reported diode laser [38] and FTS [39] measurements in better agreement with ours, yielding $\langle\gamma_m(\nu_2)/\gamma_m(\nu_1)\rangle = 0.96(6)$ for self-broadening for 14 corresponding lines. Baldacchini et al. [40] have measured the temperature dependence of the foreign-gas broadening of the $aqQ(9,9)$ transition in the ν_2 band using a diode laser. We did not scan the corresponding ν_1 transition at 3329.249 cm^{-1}, but comparing $sqQ(9,9)$ at 3331.469 cm^{-1} with their $T = 296$ K results, we obtain $\gamma_m(\nu_2)/\gamma_m(\nu_1) = 1.22(3)$, 1.04(2), 0.98(2), 0.93(2), and 0.82(4) for N_2, O_2, H_2, Ar, and He buffers, respectively.

In our previous study of self-broadening [1], we found that semiclassical Anderson–Tsao–Curnutte theory, using only dipole–dipole interactions, qualitatively describes the strong $J-K$ dependence shown in Fig. 7, but overestimates the magnitude of the self-broadening by 5–25%, depending on K. The same theory applied to NH_3–N_2 collisions [2], using only dipole–quadrupole cou-

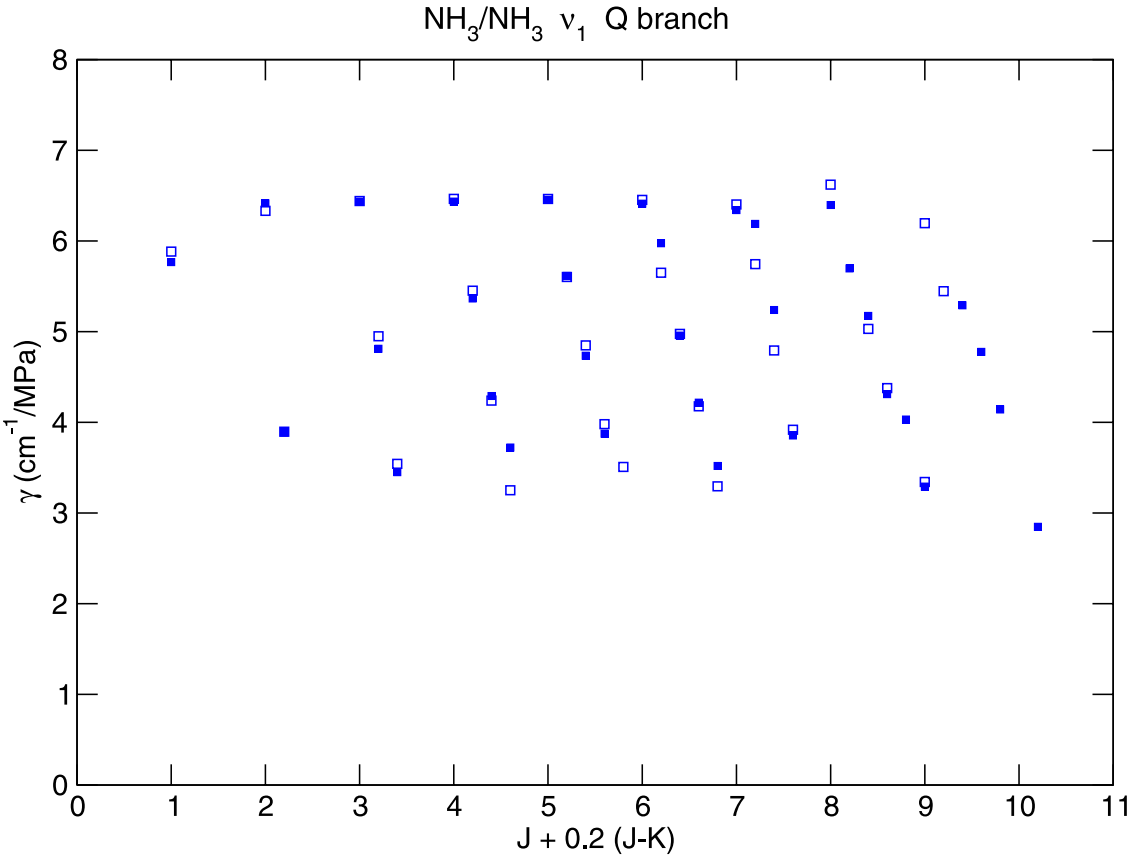

Fig. 7. Rotational dependence of self-broadening coefficients in ν_1 $qQ(J,K)$ branch of NH_3 vs. $J + 0.2\times(J-K)$. Open symbols for symmetric ground-state tunneling level, filled for antisymmetric.

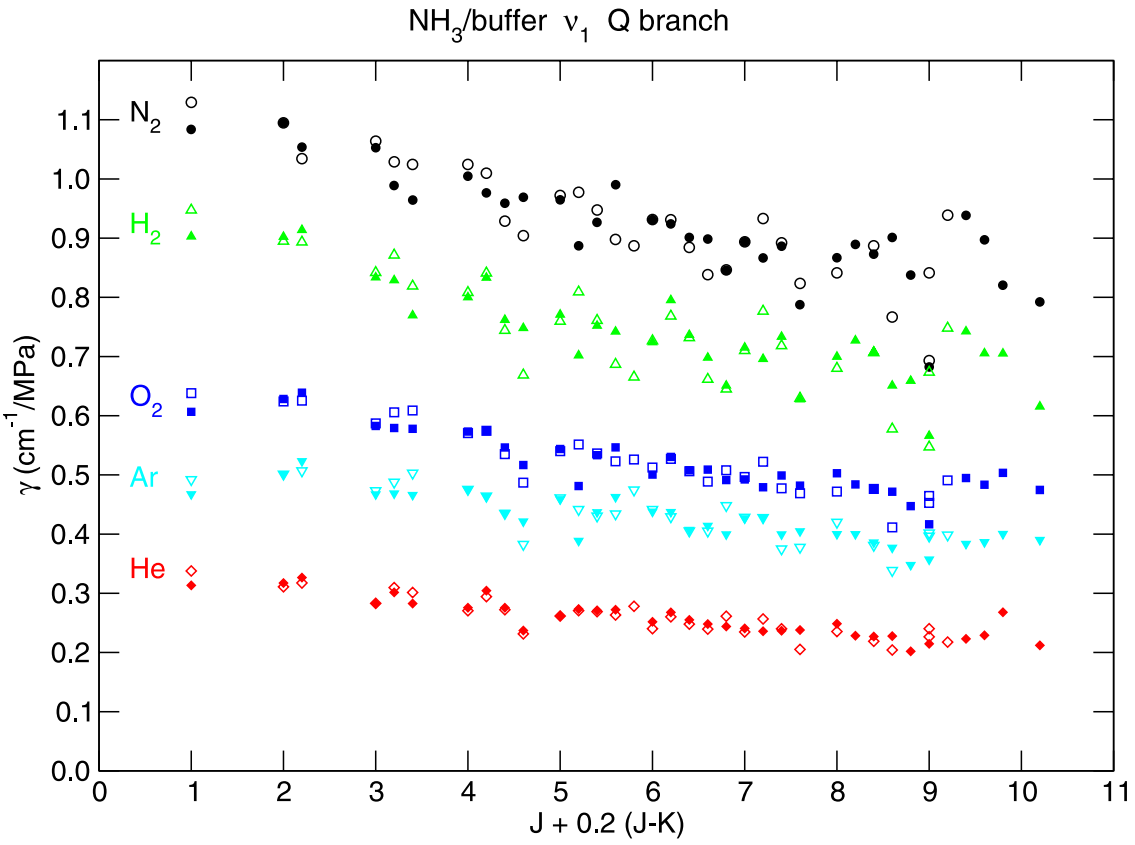

Fig. 8. Rotational dependence of foreign-gas broadening coefficients in ν_1 $qQ(J,K)$ branch of NH_3 vs. $J + 0.2 \times (J - K)$. Buffer gas indicated. Open symbols for symmetric ground-state tunneling level, filled for antisymmetric.

pling, grossly overestimates the $J - K$ dependence and yields less variation for $J = K$ than is observed for the Q branch shown in Fig. 8. A more detailed semiclassical theory [28,35] developed for linear non-polar buffer gases discusses various contributions to the broadenings in NH_3. However, this model provides only semiquantitative agreement when applied our NH_3–H_2 ν_1 Q-branch broadenings [35]. The empirical polynomial expansions of NSV [15] and BP [16] have difficulties in fitting the low J self-broadenings; and those designed to fit the ν_2 P and R branches [15] for non-polar buffers exhibit much more $J - K$ dependence than observed in the ν_1 Q branch here.

In our scans of the ν_1 Q and R branches, we have observed numerous transitions of the ν_3 and $2\nu_4$ bands, as shown in Appendix A. We list our better-determined ν_3 broadenings for the various buffers in Table 7. Since this is only a fragmentary collection, it is difficult to note any systematic trends. In most cases, the $s - a$ tunneling partners have very similar broadenings. Because ν_3 is a perpendicular band ($\Delta K = \pm 1$), a direct comparison with ν_1 is problematic. However, for the Q branches with the same J and K, we find slightly larger broadenings in ν_3. The $pP(4,2)$ lines in ν_3 are comparable to the $qR(3,2)$ lines in ν_1 for the foreign gases, but are ~15% narrower for self-broadening. This latter variation may reflect the much larger K dependence observed for self-broadening in Fig. 7. A comparison can also be made with recent measurements [28,32,35] of the $P(J,K)$ lines in the ν_4 perpendicular band. For N_2 broadening, there are 6 lines in common with an average ratio, $\langle \gamma_m(\nu_4)/\gamma_m(\nu_3) \rangle = 0.99(6)$, for O_2 there are 8 lines with $\langle \gamma_m(\nu_4)/\gamma_m(\nu_3) \rangle = 0.98(5)$, and for H_2 there are 11 lines with $\langle \gamma_m(\nu_4)/\gamma_m(\nu_3) \rangle = 1.07(5)$. Apart from the slightly broader ν_4 lines in the H_2 case, the scatter appears random and is comparable to the combined experimental errors.

10. Comparison with HITRAN2K

There have been several revisions to the HITRAN database for NH_3 since our initial reports [1,2], and the current version [14] includes the improved measurements and assignments in the 3 μm region by Kleiner et al. [13]. The wavenumbers and intensities in the database can be tested against our low-pressure spectra such as the ν_1 Q branch shown in Fig. 9. At this pressure, the spectrum is nearly Doppler limited and is insensitive to broadening or lineshape considerations. The dotted spectrum in Fig. 9 is the HITRAN2K (H2K) prediction using a Voigt profile and the unmagnified residuals are

Table 7
NH_3 ν_3 band P- and Q-branch broadening coefficients, γ_m, in cm^{-1}/MPa at $T = 296$ K in various buffer gases using the dispersive Rautian model

Line	ω_m	N_2	O_2	H_2	Ar	He	NH_3
spP(2,2)	3415.40987	1.1185(8)	0.6374(4)	0.9234(6)	0.5098(4)	0.3170(3)	6.0608(0)
srQ(7,2)	3415.34344	0.7803(22)	0.4593(12)	0.6103(16)	0.3903(10)	0.2276(7)	3.6606(172)
arQ(7,2)	3415.07909	0.7595(33)	0.4410(18)	0.5900(25)	0.3690(15)	0.2127(9)	3.3434(249)
apP(2,2)	3414.97167	1.1072(7)	0.6319(4)	0.9149(6)	0.5100(4)	0.3211(3)	5.9009(68)
srQ(4,3)	3414.69872	1.0867(24)	0.5984(12)	0.8587(18)	0.4828(10)	0.2946(6)	6.1614(268)
arQ(4,3)	3414.30977	1.0985(8)	0.6189(5)	0.8919(6)	0.5043(4)	0.3053(3)	6.1865(81)
srQ(5,3)	3412.98989	1.0121(17)	0.5526(7)	0.8042(12)	0.4390(6)	0.2759(4)	5.3342(150)
srQ(8,2)	3412.70509	0.6848(31)	0.4357(19)	0.5688(25)	0.3680(17)	0.2187(11)	3.0358(233)
arQ(5,3)	3412.62881	1.0156(7)	0.5714(4)	0.8192(5)	0.4548(3)	0.2819(3)	5.3395(61)
arQ(8,2)	3412.45112	0.6281(29)	0.3867(18)	0.5176(24)	0.3202(16)	0.1834(11)	2.9267(225)
spP(4,2)	3373.95344	1.0446(8)	0.5985(5)	0.8105(6)	0.4858(4)	0.2920(3)	4.3814(34)
apP(4,2)	3373.56726	1.0176(8)	0.5759(5)	0.7835(6)	0.4677(4)	0.2812(3)	4.3104(35)
spP(7,7)	3355.56587	0.8894(6)	0.4944(4)	0.7101(5)	0.4346(4)	0.2380(3)	6.1700(45)
apP(7,7)	3354.99260	0.8946(15)	0.5001(8)	0.7146(12)	0.4352(15)	0.2433(8)	6.2047(102)
spP(5,2)	3352.81604	0.9814(10)	0.5601(6)	0.7262(8)	0.4687(5)	0.2790(4)	4.2321(44)
srP(5,0)	3336.91070	0.9090(8)	0.5175(4)	0.6581(7)	0.4355(4)	0.2530(4)	3.5931(37)
spP(7,5)	3336.09474	0.9258(14)	0.5086(7)	0.7391(12)	0.4085(6)	0.2483(4)	5.2163(131)
apP(7,5)	3335.66907	0.9208(18)	0.5046(9)	0.7416(15)	0.4050(7)	0.2505(5)	5.2211(153)
spP(8,7)	3333.43544	0.8254(41)	0.4633(19)	0.6819(30)	0.3922(16)	0.2262(11)	5.7849(174)
apP(8,7)	3332.91588	0.9379(48)	0.5022(20)	0.7714(37)	0.4194(16)	0.2377(10)	5.5829(154)
spP(9,9)	3331.92568	0.9347(62)	0.5241(50)	0.8181(65)	0.4141(54)	0.2478(31)	5.3613(274)
spP(6,2)	3331.40979	0.8408(26)	0.4925(15)	0.6320(20)	0.4141(13)	0.2489(9)	3.8051(83)
apP(9,9)	3331.22702	0.7917(36)	0.4155(17)	0.6199(29)	0.3706(15)	0.1950(10)	6.0086(172)
apP(6,2)	3331.07115	0.7670(124)	0.4956(88)	0.6497(137)	0.4385(79)	0.2486(45)	3.7723(389)

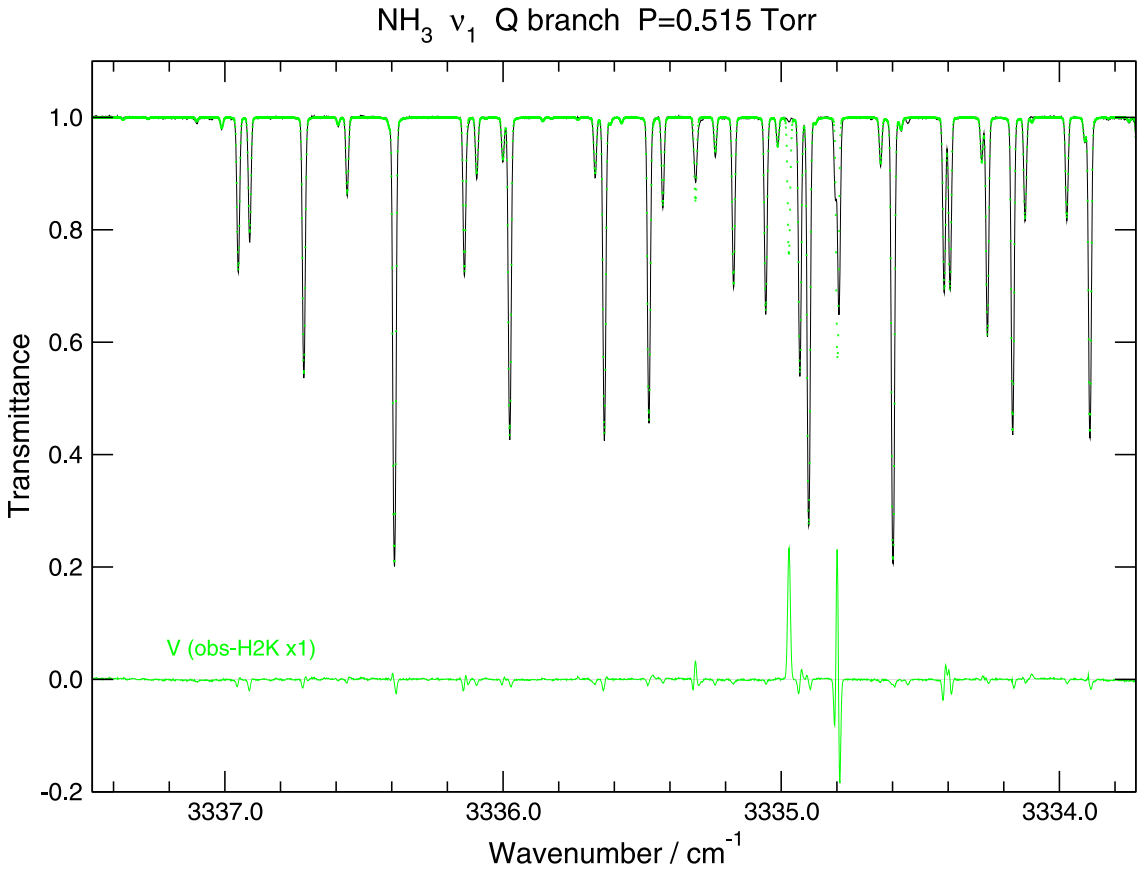

Fig. 9. Comparison of observed low pressure (0.515 Torr) trace of ν_1 $qQ(J,K)$ branch of NH_3 with HITRAN2K Voigt calculation (dotted). Residuals unmagnified.

shown below. The residuals from our parameters in Appendix A are unobservable at this scale. The large intensity deviation near 3334.97 cm^{-1} is either a typo, misprint or misassignment in H2K, and the strong positive and negative excursions near 3334.80 cm^{-1} result from a partial blend not resolved in H2K. This latter problem is common throughout the database where multiple assignments are given the same wavenumber, such as for the $aqR(0,0)$ line; but the residuals become less evident at higher pressures when the linewidths greatly exceed the splittings. The lines labeled with a question mark in Appendix A are either missing from the H2K listing or are unassigned or of doubtful assignment.

The small negative residuals for most of the lines in Fig. 9 result from systematically lower intensities in H2K than we measure here. The weighted average intensity ratio of our ν_1 band to H2K is $\langle S_m(\text{present})/S_m(\text{H2K})\rangle = 1.033(11)$ for 45 relatively unblended ν_1 Q-branch lines. This is consistent with the differences noted by Kleiner et al. [13] with our previous intensity analysis [41]. Apart from possible calibration errors, we

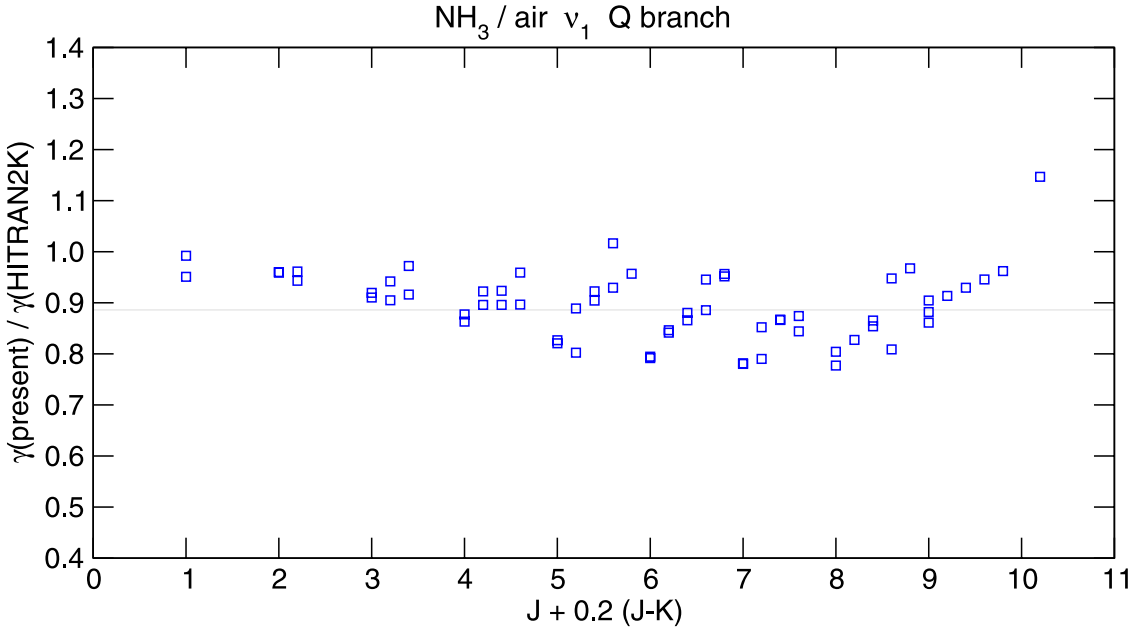

Fig. 10. Ratio of air-broadening coefficients synthesized from present γ (N_2) and γ (O_2) measurements to HITRAN2K values for ν_1 $qQ(J,K)$ branch lines of NH_3.

Table 8
Spectroscopic parameters for self-broadened NH_3 ν_1 band $R(0,0)$ manifold at $T = 296$ K using dispersive Rautian model

ω_m (cm^{-1})	S_m (cm^{-2}/MPa)	δ_m (cm^{-1}/MPa)	γ_m (cm^{-1}/MPa)	β_m (cm^{-1}/MPa)	ζ_m (1/MPa)	Assignment v^a $p\Delta K\Delta J(J,K)$
3355.99904(9)[b]	0.0385(3)	0.0(0)	3.281(31)	0.4292(0)	0.0(0)	9 $arR(5,1)$
3355.94441(7)	0.0757(5)	0.0(0)	6.144(40)	0.4292(0)	0.0(0)	9 $spQ(10,9)$
3355.69656(17)	0.0165(3)	0.0(0)	2.725(56)	0.4292(0)	0.0(0)	9 $spR(3,3)$
3355.565869(10)	0.7553(5)	−0.4534(54)	6.1700(45)	0.4292(0)	−18.532(88)	3 $spP(7,7)$
3355.330152(51)	0.1055(4)	−0.112(16)	4.492(20)	0.4292(0)	0.0(0)	9 $s?R(6,3)$
3355.26669(18)	0.0241(4)	0.0(0)	4.488(92)	0.4292(0)	0.0(0)	9 $srR(7,4)$
3355.20842(25)	0.0105(3)	0.0(0)	2.502(83)	0.4292(0)	0.0(0)	?
3355.007363(5)	1.6165(9)	1.4473(27)	3.3823(19)	0.887(23)	2.88(13)	1 $aqR(0,0)$
3354.992602(12)	0.7505(11)	0.088(12)	6.205(10)	0.4292(0)	14.28(40)	3 $apP(7,7)$
3354.90952(24)	0.0247(6)	0.0(0)	6.45(22)	0.4292(0)	0.0(0)	9 $s?R(7,5)$
3354.865765(22)	0.2688(5)	0.446(12)	4.5525(84)	0.4292(0)	−5.00(36)	8 $sqR(5,3)$
3354.104590(66)	0.0533(3)	0.0(0)	3.692(25)	0.4292(0)	0.0(0)	9 $srR(5,1)$
3353.684087(71)	0.0636(4)	0.0(0)	4.921(34)	0.4292(0)	0.0(0)	9 $a?R(6,3)$
3353.498285(40)	0.1306(3)	−0.430(16)	4.226(13)	0.4292(0)	2.77(30)	?
3352.816045(13)	0.4167(4)	0.0081(53)	4.2321(44)	0.4292(0)	−5.306(92)	3 $spP(5,2)$
3352.439104(0)	0.4159(0)	0.0(0)	4.2322(0)	0.4292(0)	5.1680(0)	3 $apP(5,2)$

[a] Vibrational code: 1 = ν_1, 3 = ν_3, 8 = $2\nu_4(A)$, 9 = $2\nu_4(E)$.
[b] Uncertainties in parentheses are one standard deviation in terms of last digits; (0) = fixed.

believe our data are more precise. The strong, isolated $aqQ(6,6)$ line at 3333.025 cm^{-1} is omitted from the ratio since its intensity is only ~77% that of $sqQ(6,6)$ in H2K.

Since we have not recorded an air-broadened spectrum, we cannot compare the H2K simulations to our spectra directly. However, we can estimate the air-

Table 9
Spectroscopic parameters for self-broadened NH_3 ν_1 band $R(1,K)$ manifold at $T = 296$ K using dispersive Rautian model

ω_m (cm^{-1})	S_m (cm^{-2}/MPa)	δ_m (cm^{-1}/MPa)	γ_m (cm^{-1}/MPa)	β_m (cm^{-1}/MPa)	ζ_m (1/MPa)	Assignment $v\ p\Delta K\Delta J(J,K)$
3376.73993(36)	0.0059(2)	0.0(0)	2.513(106)	0.4292(0)	0.0(0)	?
3376.41189(22)	0.0158(4)	0.0(0)	4.160(104)	0.4292(0)	0.0(0)	3 $srQ(10,7)$
3376.35283(16)	0.0298(6)	0.0(0)	5.325(139)	0.4292(0)	0.0(0)	?
3376.325910(6)	1.2036(7)	0.4106(45)	5.1783(42)	0.244(40)	−2.139(120)	1 $sqR(1,1)$
3376.269719(2)	3.1094(6)	0.0156(12)	2.6065(9)	0.7560(97)	−0.265(38)	1 $sqR(1,0)$
3376.16071(25)	0.0172(4)	0.0(0)	5.572(152)	0.4292(0)	0.0(0)	9 $a?R(4,3)$
3376.03858(22)	0.0168(3)	0.0(0)	4.758(103)	0.4292(0)	0.0(0)	3 $arQ(10,7)$
3375.38040(18)	0.0259(3)	0.0(0)	6.280(94)	0.4292(0)	0.0(0)	9 $arR(9,6)$
3375.07759(20)	0.0119(2)	0.0(0)	2.900(64)	0.4292(0)	0.0(0)	?
3374.84262(15)	0.0193(2)	−1.349(30)	2.225(30)	0.4292(0)	0.0(0)	?
3374.80508(11)	0.0197(2)	0.0(0)	2.392(36)	0.4292(0)	0.0(0)	?
3374.551233(5)	1.1691(4)	−0.0248(24)	5.1817(22)	0.367(38)	2.861(34)	1 $aqR(1,1)$
3374.470181(75)	0.0515(4)	0.0(0)	4.784(37)	0.4292(0)	0.0(0)	?
3374.15723(16)	0.0278(4)	0.0(0)	6.056(90)	0.4292(0)	0.0(0)	3 $srQ(9,8)$
3373.953437(10)	0.5321(4)	0.0847(45)	4.3814(34)	0.4292(0)	−6.506(82)	3 $spP(4,2)$
3373.91141(23)	0.0138(4)	0.0(0)	3.579(100)	0.4292(0)	0.0(0)	?
3373.76543(21)	0.0294(6)	0.0(0)	9.118(202)	0.4292(0)	0.0(0)	3 $arQ(9,8)$
3373.717204(16)	0.2378(4)	0.0(0)	4.2997(72)	0.4292(0)	1.125(134)	8 $aqR(6,3)$
3373.567257(10)	0.5009(4)	0.0168(47)	4.3104(35)	0.4292(0)	6.484(99)	3 $apP(4,2)$
3373.44421(29)	0.0142(3)	0.0(0)	5.0000(0)	0.4292(0)	0.0(0)	9 $srR(9,6)$
3373.40983(33)	0.0124(3)	0.0(0)	5.0000(0)	0.4292(0)	0.0(0)	9 $apR(4,2)$
3373.090737(0)	0.0114(0)	0.0(0)	5.0000(0)	0.4292(0)	0.0(0)	3 $srQ(11,7)$

Table 10
Spectroscopic parameters for self-broadened NH_3 ν_1 band $R(3,K)$ manifold at $T = 296$ K using dispersive Rautian model

ω_m (cm^{-1})	S_m (cm^{-2}/MPa)	δ_m (cm^{-1}/MPa)	γ_m (cm^{-1}/MPa)	β_m (cm^{-1}/MPa)	ζ_m (1/MPa)	Assignment $v\ p\Delta K\Delta J(J,K)$
3415.583503(0)	0.0704(0)	−0.2498(0)	4.3837(0)	0.4292(0)	0.0(0)	8 $aqR(8,5)$
3415.498857(0)	0.0413(0)	−2.3040(0)	5.9639(0)	0.4292(0)	0.0(0)	8 $aqR(9,9)$
3415.433295(0)	0.0352(0)	2.7628(0)	6.2645(0)	0.4292(0)	0.0(0)	0 $aqR(9,9)$
3415.409870(0)	0.6615(0)	−0.0652(0)	6.0608(0)	0.4292(0)	−15.92(0)	3 $spP(2,2)$
3415.343440(50)	0.1075(4)	−0.395(14)	3.6606(172)	0.4292(0)	0.0(0)	3 $srQ(7,2)$
3415.28200(21)	0.0186(3)	0.847(46)	2.3623(509)	0.4292(0)	0.0(0)	9 $a?R(9,4)$
3415.105245(5)	2.1576(9)	0.1832(37)	6.1386(28)	0.161(42)	−3.755(59)	1 $sqR(3,3)$
3415.079090(46)	0.1020(7)	0.0(0)	3.3434(249)	0.4292(0)	0.0(0)	3 $arQ(7,2)$
3414.971665(13)	0.6508(6)	−0.059(10)	5.9009(68)	0.4292(0)	14.31(22)	3 $apP(2,2)$
3414.832639(5)	1.6910(7)	0.1239(37)	4.9355(26)	0.311(35)	−2.370(84)	1 $sqR(3,2)$
3414.698720(23)	0.4713(14)	−0.114(25)	6.1614(268)	0.4292(0)	−13.26(1.49)	3 $srQ(4,3)$
3414.683486(6)	2.0005(13)	0.0893(56)	3.7606(40)	0.356(27)	−2.11(36)	1 $sqR(3,1)$
3414.636264(3)	4.1835(11)	0.0260(21)	3.0630(16)	0.499(14)	−0.050(76)	1 $sqR(3,0)$
3414.36035(19)	0.0154(4)	0.0(0)	2.4391(654)	0.4292(0)	0.0(0)	9 $apR(6,1)$
3414.309766(17)	0.4754(6)	0.3419(99)	6.1865(81)	0.4292(0)	13.79(15)	3 $arQ(4,3)$
3413.62228(27)	0.0085(2)	0.0(0)	2.0222(758)	0.4292(0)	0.0(0)	8 $sqR(8,1)$
3413.54189(18)	0.0163(3)	0.0(0)	2.6301(612)	0.4292(0)	0.0(0)	3 $srQ(10,1)$
3413.42045(29)	0.0078(3)	0.0(0)	1.8268(872)	0.4292(0)	0.0(0)	3 $arQ(10,1)$
3413.320502(5)	2.1423(7)	−0.0663(31)	6.2098(25)	0.215(43)	3.913(51)	1 $aqR(3,3)$
3413.087370(5)	1.7130(7)	−0.1568(35)	4.9426(25)	0.025(33)	2.740(84)	1 $aqR(3,2)$
3412.989887(17)	0.5140(8)	−0.1981(155)	5.3342(150)	0.4292(0)	−11.77(96)	3 $srQ(5,3)$
3412.959155(4)	1.9756(8)	−0.1412(35)	3.7425(23)	0.281(23)	−0.32(20)	1 $aqR(3,1)$
3412.705086(62)	0.0562(4)	0.0(0)	3.0358(233)	0.4292(0)	0.0(0)	3 $srQ(8,2)$
3412.628815(14)	0.5172(5)	0.2239(76)	5.3395(61)	0.4292(0)	12.47(14)	3 $arQ(5,3)$
3412.451120(64)	0.0512(3)	0.0(0)	2.9267(225)	0.4292(0)	0.0(0)	3 $arQ(8,2)$
3412.37816(69)	0.0083(5)	0.0(0)	5.644(363)	0.4292(0)	0.0(0)	9 $s?R(5,4)$
3411.192717(0)	0.0856(0)	0.0(0)	3.5241(0)	0.4292(0)	0.0(0)	8 $aqR(8,0)$

Table 11
Spectroscopic parameters for self-broadened NH_3 ν_1 band Q branch at $T = 296$ K using dispersive Rautian model

ω_m (cm^{-1})	S_m (cm^{-2}/MPa)	δ_m (cm^{-1}/MPa)	γ_m (cm^{-1}/MPa)	β_m (cm^{-1}/MPa)	ζ_m (1/MPa)	Assignment $v\ p\Delta K\Delta J(J,K)$
3337.36529(38)	0.0139(6)	0.0(0)	5.26(24)	0.4292(0)	0.0(0)	?
3337.27462(49)	0.0118(6)	0.0(0)	6.23(35)	0.4292(0)	0.0(0)	9 *sqR*(3,1)
3337.10109(18)	0.0311(6)	−0.115(67)	4.578(84)	0.4292(0)	0.0(0)	9 *a?Q*(10,7)
3337.01132(11)	0.0626(7)	0.349(73)	6.065(79)	0.4292(0)	0.0(0)	9 *spQ*(8,8)
3336.951741(8)	1.0812(8)	0.2977(75)	5.8831(60)	0.260(74)	−2.88(18)	1 *sqQ*(1,1)
3336.910705(8)	0.8106(6)	−0.0395(33)	3.5931(37)	0.386(41)	0.0(0)	3 *srP*(5,0)
3336.716032(5)	2.0829(9)	0.1737(44)	6.3318(31)	0.548(52)	−4.21(10)	1 *sqQ*(2,2)
3336.59261(11)	0.0545(6)	−0.177(55)	4.050(58)	0.4292(0)	0.0(0)	9 *a?R*(4,1)
3336.560233(12)	0.4914(6)	−0.0168(57)	3.8962(70)	0.384(72)	0.0(0)	1 *sqQ*(2,1)
3336.40788(19)	0.0324(8)	0.0(0)	4.0(0)	0.4292(0)	0.0(0)	9 *srR*(7,5)
3336.390403(3)	5.3665(16)	0.0431(28)	6.4411(21)	0.503(36)	−3.874(45)	1 *sqQ*(3,3)
3336.138984(8)	1.0951(11)	−0.1061(38)	4.9486(47)	0.482(61)	0.0(0)	1 *sqQ*(3,2)
3336.12595(24)	0.0318(10)	0.0(0)	5.0(0)	0.4292(0)	0.0(0)	?
3336.094736(18)	0.3861(7)	−0.519(12)	5.216(13)	0.4292(0)	0.0(0)	3 *spP*(7,5)
3336.000792(23)	0.2714(8)	−0.115(13)	3.542(13)	0.4292(0)	0.0(0)	1 *sqQ*(3,1)
3335.975919(4)	2.8562(12)	0.0279(43)	6.4642(36)	0.540(47)	−5.019(84)	1 *sqQ*(4,4)
3335.86009(24)	0.0207(6)	0.0(0)	4.57(16)	0.4292(0)	0.0(0)	9 *a?Q*(10,6)
3335.82494(47)	0.0074(5)	0.0(0)	2.84(21)	0.4292(0)	0.0(0)	1 *sqQ*(9,2)
3335.669073(19)	0.3769(8)	0.057(14)	5.221(15)	0.4292(0)	0.0(0)	3 *apP*(7,5)
3335.635803(4)	2.8156(12)	−0.1136(24)	5.4518(31)	0.639(37)	0.0(0)	1 *sqQ*(4,3)
3335.61337(18)	0.0332(7)	0.0(0)	5.0(0)	0.4292(0)	0.0(0)	1 *sqQ*(9,3)
3335.57351(15)	0.0429(5)	−0.305(96)	5.0(0)	0.4292(0)	0.0(0)	1 *sqQ*(9,4)
3335.475653(4)	2.6252(11)	0.0242(44)	6.4630(36)	0.607(49)	−6.90(10)	1 *sqQ*(5,5)
3335.425592(12)	0.5632(7)	−0.0258(68)	4.2393(78)	0.341(76)	0.0(0)	1 *sqQ*(4,2)
3335.31340(9)	0.1480(36)	−0.030(23)	3.251(31)	0.60(22)	0.0(0)	1 *sqQ*(4,1)
3335.30645(5)	0.3537(33)	0.048(28)	6.249(41)	0.4292(0)	0.0(0)	?
3335.29002(17)	0.0310(9)	0.0(0)	4.06(13)	0.4292(0)	0.0(0)	9 *s?Q*(9,9)
3335.236713(28)	0.2381(7)	0.274(17)	5.199(20)	0.4292(0)	0.0(0)	?
3335.171223(7)	1.2008(9)	−0.2398(69)	5.7674(54)	0.435(67)	2.73(19)	1 *aqQ*(1,1)
3335.055624(6)	1.4242(9)	−0.0921(42)	5.6033(51)	0.215(56)	0.0(0)	1 *sqQ*(5,4)
3335.01271(4)	0.1749(8)	0.056(32)	5.446(36)	0.4292(0)	0.0(0)	1 *sqQ*(9,8)
3334.97146(16)	0.0339(6)	0.0(0)	5.0000(0)	0.4292(0)	0.0(0)	?
3334.932955(5)	2.0701(13)	−0.078(10)	6.415(11)	0.637(76)	−4.06(87)	1 *aqQ*(2,2)
3334.901136(3)	4.3599(18)	−0.0035(63)	6.4535(58)	0.530(47)	−2.88(41)	1 *sqQ*(6,6)
3334.87640(19)	0.0326(8)	0.0(0)	5.0000(0)	0.4292(0)	0.0(0)	9 *apR*(3,1)
3334.805480(18)	0.4863(12)	−0.205(13)	3.888(17)	−0.01(11)	0.0(0)	1 *aqQ*(2,1)
3334.792485(7)	1.4229(13)	−0.0533(60)	4.8489(80)	0.622(62)	0.0(0)	1 *sqQ*(5,3)
3334.642712(23)	0.2922(8)	−0.048(15)	3.980(16)	0.4292(0)	0.0(0)	1 *sqQ*(5,2)
3334.598223(3)	5.3119(17)	−0.1416(33)	6.4329(29)	0.638(38)	5.626(65)	1 *aqQ*(3,3)
3334.56833(9)	0.0731(8)	0.121(61)	3.508(64)	0.4292(0)	0.0(0)	1 *sqQ*(5,1)
3334.54524(18)	0.0305(6)	0.0(0)	5.0(0)	0.4292(0)	0.0(0)	?
3334.414332(7)	1.2434(10)	−0.0587(63)	5.6498(76)	−0.024(68)	0.0(0)	1 *sqQ*(6,5)
3334.393126(7)	1.2258(10)	−0.0683(52)	4.8115(61)	−0.423(49)	0.0(0)	1 *aqQ*(3,2)
3334.279494(24)	0.2565(8)	−0.092(14)	3.451(14)	0.4292(0)	0.0(0)	1 *aqQ*(3,1)
3334.258896(6)	1.6399(11)	−0.0823(79)	6.4029(65)	0.367(68)	−3.74(21)	1 *sqQ*(7,7)
3334.167961(4)	2.7986(11)	−0.0793(48)	6.4338(38)	0.271(46)	5.10(12)	1 *aqQ*(4,4)
3334.123314(11)	0.6711(8)	−0.0813(78)	4.9758(88)	0.436(89)	0.0(0)	1 *sqQ*(6,4)
3333.973560(10)	0.6629(6)	−0.1496(43)	4.1761(53)	0.286(53)	0.0(0)	1 *sqQ*(6,3)
3333.909006(36)	0.1375(8)	0.0(0)	3.294(26)	0.4292(0)	0.0(0)	1 *sqQ*(6,2)
3333.890330(4)	2.8214(11)	−0.0898(34)	5.3653(25)	0.248(30)	4.304(75)	1 *aqQ*(4,3)
3333.74870(19)	0.0234(0)	0.0(0)	4.0(0)	0.4292(0)	0.0(0)	1 *sqQ*(8,2)
3333.718262(9)	0.5509(6)	0.0(0)	4.2908(66)	0.811(71)	0.0(0)	1 *aqQ*(4,2)
3333.644402(5)	2.5880(12)	−0.1309(49)	6.4537(39)	0.445(46)	8.12(13)	1 *aqQ*(5,5)
3333.62596(4)	0.1503(9)	0.0(0)	3.722(30)	0.4292(0)	0.0(0)	1 *aqQ*(4,1)
3333.58927(5)	0.1134(9)	0.0(0)	3.343(33)	0.4292(0)	0.0(0)	1 *sqQ*(8,3)
3333.572980(6)	1.6714(11)	−0.1792(49)	5.7441(53)	0.562(54)	0.0(0)	1 *sqQ*(7,6)
3333.509882(12)	1.0615(18)	0.315(14)	6.622(13)	2.22(16)	−21.722(33)	1 *sqQ*(8,8)
3333.499202(19)	0.5498(18)	0.0(0)	4.792(14)	0.4292(0)	0.0(0)	1 *sqQ*(7,5)
3333.45230(10)	0.0486(7)	0.0(0)	3.603(65)	0.4292(0)	0.0(0)	1 *sqQ*(7,2)
3333.435442(22)	0.3748(11)	0.0(0)	5.785(17)	0.4292(0)	0.0(0)	3 *spP*(8,7)
3333.421095(33)	0.2001(10)	0.0(0)	4.378(22)	0.4292(0)	0.0(0)	1 *sqQ*(8,5)

(*continued on next page*)

Table 11 (*continued*)

ω_m (cm^{-1})	S_m (cm^{-2}/MPa)	δ_m (cm^{-1}/MPa)	γ_m (cm^{-1}/MPa)	β_m (cm^{-1}/MPa)	ζ_m (1/MPa)	Assignment $v\ p\Delta K\Delta J(J,K)$
3333.40009(19)	0.1157(1)	0.0(0)	3.9188(51)	0.4292(0)	0.0(0)	1 *sqQ*(8,4)
3333.39830(9)	0.2828(3)	0.0(0)	3.9188(51)	0.4292(0)	0.0(0)	1 *sqQ*(7,4)
3333.39436(4)	0.2809(3)	0.0(0)	3.9188(51)	0.4292(0)	0.0(0)	1 *sqQ*(7,3)
3333.32212(22)	0.0279(7)	0.0(0)	5.0(0)	0.4292(0)	0.0(0)	9 *aqR*(3,1)
3333.303919(15)	1.3831(7)	0.0(0)	5.6148(30)	−0.378(60)	5.233(82)	1 *aqQ*(5,4)
3333.301403(30)	0.6550(3)	0.0(0)	5.6148(30)	0.4292(0)	0.0(0)	1 *sqQ*(8,7)
3333.086191(6)	1.4068(8)	0.0486(33)	4.7347(39)	0.575(39)	0.0(0)	1 *aqQ*(5,3)
3333.024970(3)	4.2609(12)	−0.0808(28)	6.4110(25)	0.547(34)	8.804(53)	1 *aqQ*(6,6)
3332.961916(17)	0.2914(7)	0.0(0)	3.876(12)	0.4292(0)	0.0(0)	1 *aqQ*(5,2)
3332.938091(9)	0.7038(9)	0.0(0)	5.0301(78)	−0.123(70)	0.0(0)	1 *sqQ*(8,6)
3332.915885(19)	0.3723(10)	0.0(0)	5.583(15)	0.4292(0)	0.0(0)	3 *apP*(8,7)
3332.89968(7)	0.0655(7)	0.0(0)	3.112(36)	0.4292(0)	0.0(0)	1 *aqQ*(5,1)
3332.87265(4)	0.1414(6)	0.0(0)	4.843(24)	0.4292(0)	0.0(0)	8 *sqR*(4,2)
3332.76473(13)	0.0319(3)	0.0(0)	4.0(0)	0.4292(0)	0.0(0)	9 *spR*(3,1)
3332.639952(15)	1.2353(35)	0.2723(42)	5.9754(92)	1.70(11)	0.0(0)	1 *aqQ*(6,5)
3332.631705(31)	0.5315(35)	0.0(0)	5.571(19)	0.4292(0)	0.0(0)	?
3332.398279(11)	0.6611(7)	0.0624(57)	4.9568(62)	0.281(71)	0.0(0)	1 *aqQ*(6,4)
3332.348617(6)	1.6298(8)	−0.0554(53)	6.3404(43)	0.039(52)	9.36(12)	1 *aqQ*(7,7)
3332.29562(3)	0.1768(8)	0.0(0)	5.291(32)	0.4292(0)	0.0(0)	1 *aqQ*(9,7)
3332.270094(11)	0.7311(9)	0.0810(63)	4.2173(57)	−0.057(51)	0.0(0)	1 *aqQ*(6,3)
3332.253746(28)	0.2460(9)	0.0(0)	5.598(28)	0.4292(0)	0.0(0)	?
3332.21190(3)	0.1366(6)	0.0(0)	3.519(16)	0.4292(0)	0.0(0)	1 *aqQ*(6,2)
3332.18984(5)	0.0730(5)	0.0(0)	2.848(20)	0.4292(0)	0.0(0)	1 *aqQ*(9,3)
3332.13408(8)	0.0500(5)	0.0(0)	4.031(44)	0.4292(0)	0.0(0)	1 *aqQ*(9,4)
3331.92568(3)	0.8178(9)	−0.3249(44)	5.361(27)	0.38(11)	0.0(0)	3 *spP*(9,9)
3331.922898(11)	1.8105(0)	0.0(0)	6.188(16)	0.4292(0)	0.0(0)	1 *aqQ*(7,6)
3331.82102(6)	0.0674(5)	0.0(0)	4.141(36)	0.4292(0)	0.0(0)	1 *aqQ*(9,5)
3331.738635(19)	0.2759(7)	0.0(0)	4.777(13)	0.4292(0)	0.0(0)	1 *aqQ*(9,6)
3331.713548(11)	0.5367(8)	0.0(0)	5.2387(84)	1.08(11)	0.0(0)	1 *aqQ*(7,5)
3331.672990(28)	0.2106(8)	0.0(0)	5.890(26)	0.4292(0)	0.0(0)	?
3331.628671(19)	1.0919(46)	−0.003(11)	6.396(16)	0.59(11)	13.90(19)	1 *aqQ*(8,8)
3331.62280(19)	0.0689(48)	0.0(0)	3.116(82)	0.4292(0)	0.0(0)	1 *aqQ*(7,2)
3331.60483(4)	0.2899(17)	0.0(0)	4.434(19)	0.4292(0)	0.0(0)	1 *aqQ*(7,3)
3331.59543(3)	0.2920(17)	0.0(0)	3.855(14)	0.4292(0)	0.0(0)	1 *aqQ*(7,4)
3331.469240(8)	1.1316(7)	0.1687(63)	6.1964(45)	−0.060(63)	−7.92(16)	1 *sqQ*(9,9)
3331.409795(16)	0.2715(5)	0.0(0)	3.8051(83)	0.4292(0)	0.0(0)	3 *spP*(6,2)
3331.35878(3)	0.1127(5)	0.0(0)	3.291(15)	0.4292(0)	0.0(0)	1 *aqQ*(8,3)
3331.23942(5)	0.1154(8)	0.0(0)	4.0305(0)	0.4292(0)	0.0(0)	1 *aqQ*(8,4)
3331.22702(2)	0.4193(11)	0.0(0)	6.009(17)	0.4292(0)	0.0(0)	3 *apP*(9,9)
3331.207841(12)	0.7276(10)	0.122(12)	5.9882(93)	−0.187(96)	13.37(20)	?
3331.177954(14)	0.4383(7)	0.0(0)	5.697(12)	0.4292(0)	0.0(0)	1 *aqQ*(8,7)
3331.07115(16)	0.163(11)	0.0(0)	3.772(39)	0.4292(0)	0.0(0)	3 *apP*(6,2)
3331.06660(10)	0.301(11)	0.0(0)	4.310(28)	0.4292(0)	0.0(0)	1 *aqQ*(8,5)
3331.037632(10)	0.6702(7)	0.2298(48)	5.1740(56)	0.068(72)	0.0(0)	1 *aqQ*(8,6)
3330.84391(27)	0.0181(5)	0.0(0)	5.10(15)	0.4292(0)	0.0(0)	?

broadening coefficients from our N_2 and O_2 values and the standard composition of air,

$$\gamma_m(\text{air}) = 0.79\gamma_m(N_2) + 0.21\gamma_m(O_2), \tag{11}$$

for comparison to the H2K parameters. For the *R*-branch lines given in Table 5, we obtain excellent agreement, with an average ratio of $\langle \gamma_m(\text{air, present})/\gamma_m(\text{air,H2K})\rangle = 0.992(16)$. However, we see some systematic deviations in the ratios for the *Q*-branch lines as shown in Fig. 10. Here we obtain a weighted average air-broadening ratio of $\langle \gamma_m(\text{air, present})/\gamma_m(\text{air, H2K})\rangle = 0.886(64)$ for the well-determined set of *Q*-branch lines in Table 10. The sawtooth appearance of the points in Fig. 10 indicates that the $J - K$ dependence of the H2K modeling [14,15] is significantly larger than we observe for either N_2 or O_2 broadening as shown in Fig 8. The offset of the average is also much larger than the self-broadening correction applied here. Moreover, there is a systematic parabolic deviation for the $J = K$ values. Therefore, improvements are required for the ν_1 *Q*-branch database.

11. Conclusions

Using a multiple-spectrum fitting procedure, we have obtained improved precision for transition intensities, broadenings and shifts in the *Q* and *R* branches of the

v_1 band of NH_3 for a variety of buffer gases. Generally, we have shown that the conventional Voigt profile leaves residuals of 1–2% at pressures where the broadenings are comparable to the Doppler width. These residuals can be greatly reduced by taking Dicke narrowing and/or speed-dependent broadening into account. These latter two effects cannot be distinguished for the present data; higher signal-to-noise and a wider pressure and temperature range may help. For Dicke narrowing, the Rautian hard-collision model is generally sufficient, though the Galatry soft-collision model fits slightly better for He broadening. For speed-dependent broadening, the $V(R) \propto R^{-q}$ model of Berman [9] and Ward et al. [10] provides some physical insight, though it fails for NH_3–He where a simple quadratic speed dependence [11] fits well.

At the higher pressures measured, it was necessary to include line mixing to first order. The contribution of line mixing is manifest in the residuals from spectra projected without line mixing. These residuals dramatically reveal the collisional propensity rules which differ markedly for self and foreign-gas buffers. Collisional tunneling transitions dominate for the dipole–dipole interaction for self-broadening, whereas $\Delta K = \pm 3$ transitions dominate for the Ar, He and O_2 buffers.

Previous semiclassical theoretical models qualitatively describe the self-broadenings [1] but strongly exaggerate the $J - K$ dependence for the non-polar buffers [2,28,34]. Empirical polynomial models [15,16] based only on J and K also have difficulty representing self-broadening at low J, and the Q-branch broadenings for non-polar buffer gases. Among parallel bands, we find very little vibrational dependence except for self-broadening in the v_2 umbrella mode ladder, again consistent with the tunneling propensity for dipole–dipole interaction. Perpendicular bands are similar to each other and to parallel bands of the same J and K ($J - 1$ for R-branch lines) with the exception of the strongly K-dependent self-broadening.

The HITRAN database for NH_3 has been improved with the inclusion of more recent spectra [13–16] but still needs to be purged of obvious intensity errors and could use higher resolution data for the partial blends. The rotational modeling of the broadenings needs to take the branch and band type into account and corrections to the Voigt profile due to Dicke narrowing and line mixing are essential over the atmospheric pressure range. Assignments in the N–H stretching region are particularly difficult due to strong perturbations [12,13], but high-resolution temperature-dependent studies may help to yield ground-state energies and hot bands.

Acknowledgments

The authors are grateful to L.R. Brown for providing NH_3 listings and spectra from [13] and to R. Ciurylo and T. Gabard for helpful discussions regarding lineshapes and line-mixing selection rules.

Appendix A

Wavenumbers, intensities, assignments, and self-broadening parameters for transitions in the $R(0)$, $R(1)$, and $R(3)$ manifolds and Q branch in the v_1 band of NH_3 at $T = 296\,K$ are listed in Tables 8–11 above. Foreign-gas-broadening parameters are available from the corresponding author or the journal archive.

Appendix B. Supplementary data

Supplementary data for this article are available on ScienceDirect (www.sciencedirect.com) and as part of the Ohio State University Molecular Spectroscopy Archives (http://msa.lib.ohio-state.edu/jmsa_hp.htm).

References

[1] V.N. Markov, A.S. Pine, G. Buffa, O. Tarrini, J. Quant. Spectrosc. Radiat. Transfer 50 (1993) 167–178.
[2] A.S. Pine, V.N. Markov, G. Buffa, O. Tarrini, J. Quant. Spectrosc. Radiat. Transfer 50 (1993) 337–348.
[3] S.G. Rautian, I.I. Sobel'man, Sov. Phys. Uspheki 9 (1967) 701–716.
[4] L. Galatry, Phys. Rev. 122 (1961) 1218–1223.
[5] D.C Benner, C.P. Rinsland, V.M. Devi, M.A.H. Smith, D. Atkins, J. Quant. Spectrosc. Radiat. Transfer 53 (1995) 705–721.
[6] A.S. Pine, T. Gabard, J. Quant. Spectrosc. Radiat. Transfer 66 (2000) 69–92.
[7] A.S. Pine, T. Gabard, J. Mol. Spectrosc. 217 (2003) 105–114.
[8] J.W. Brault, L.R. Brown, C. Chackerian, R. Freedman, A. Predoi-Cross, A.S. Pine, J. Mol. Spectrosc. 222 (2003) 220–239.
[9] P.R. Berman, J. Quant. Spectrosc. Radiat. Transfer 12 (1972) 1331–1342.
[10] J. Ward, J. Cooper, E.W. Smith, J. Quant. Spectrosc. Radiat. Transfer 14 (1974) 555–590.
[11] D. Priem, F. Rohart, J.-M. Colmont, G. Wlodarczak, J. Mol. Struct. 517 (2000) 435–454.
[12] R. Angstl, H. Finsterholzl, F. Frunder, D. Illig, P. Papousek, P. Pracna, K.N. Rao, H. Schrotter, S. Urban, J. Mol. Spectrosc. 114 (1985) 454–472.
[13] I. Kleiner, L.R. Brown, G. Tarrago, Q.-L. Kou, N. Picque, G. Guelachvili, V. Dana, J.-Y. Mandin, J. Mol. Spectrosc. 193 (1999) 46–71.
[14] I. Kleiner et al., J. Quant. Spectrosc. Radiat. Transfer 82 (2003) 293–312.
[15] V. Nemtchinov, K. Sung, P. Varanasi, J. Quant. Spectrosc. Radiat. Transfer 83 (2004) 243–265.
[16] L.R. Brown, D.B. Peterson, J. Mol. Spectrosc. 168 (1994) 593–606.
[17] P.W. Rosenkranz, IEEE Trans. Antennas Propag. AP-23 (1975) 498–506.
[18] R. Ciurylo, A.S. Pine, J. Szudy, J. Quant. Spectrosc. Radiat. Transfer 68 (2001) 257–271.
[19] R. Ciurylo, A.S. Pine, J. Quant. Spectrosc. Radiat. Transfer 67 (2000) 375–393.

[20] I. Shannon, M. Harris, D.R. McHugh, E.L. Lewis, J. Phys. B 19 (1986) 1409–1424.
[21] A.S. Pine, J. Quant. Spectrosc. Radiat. Transfer 57 (1997) 145–155 157-176.
[22] J. Humlicek, J. Quant. Spectrosc. Radiat. Transfer 21 (1979) 309–313.
[23] S. Green, J. Hutson, J. Chem. Phys. 100 (1994) 891–898.
[24] A.S. Pine, J. Quant. Spectrosc. Radiat. Transfer 62 (1999) 397–423;
A.S. Pine, R. Ciurylo, J. Mol. Spectrosc. 208 (2001) 180–187.
[25] R. Wehr, A. Vitcu, R. Ciurylo, F. Thibault, J.R. Drummond, A.D. May, Phys. Rev. A 66 (2002) 062502-1-7.
[26] M. Abramowitz, I.A. Stegun, Handbook of Mathematical Functions, Wiley, New York, 1972 pp. 503-535.
[27] H.M. Pickett, J. Chem. Phys. 73 (1980) 6090–6094.
[28] M. Dhib, J.P. Bouanich, H. Aroui, A. Picard-Bersellini, J. Quant. Spectrosc. Radiat. Transfer 68 (2001) 163–178.
[29] A. Lightman, A. Ben-Reuven, J. Quant. Spectrosc. Radiat. Transfer 12 (1972) 449–454.
[30] S.A. Henck, K.K. Lehmann, Chem. Phys. Lett. 144 (1988) 281–285.
[31] M. Broquier, A. Picard-Bersellini, Chem. Phys. Lett. 121 (1985) 437–439.
[32] H. Aroui, M. Broquier, A. Picard-Bersellini, J.P. Bouanich, M. Chevalier, S. Gherissi, J. Quant. Spectrosc. Radiat. Transfer 60 (1998) 1011–1023 and references therein..
[33] S. Hadded, H. Aroui, J. Orphal, J.P. Bouanich, J.M. Hartmann, J. Mol. Spectrosc. 210 (2001) 275–283.
[34] S. Hadded, F. Thibault, P.M. Flaud, H. Aroui, J.M. Hartmann, J. Chem. Phys. 116 (2002) 7544–7557 120 (2004) 217–223.
[35] J.P. Bouanich, H. Aroui, S. Nouri, A. Picard-Bersellini, J. Mol. Spectrosc. 206 (2001) 104–110.
[36] C. Cottaz, G. Tarrago, I. Kleiner, L.R. Brown, J. Mol. Spectrosc. 209 (2001) 30–49.
[37] M. Fabian, F. Ito, K.M.T. Yamada, J. Mol. Spectrosc. 173 (1995) 591–602.
[38] M. Fabian, R. Schieder, K.M.T. Yamada, G. Winnerwisser, J. Mol. Spectrosc. 177 (1996) 294–301.
[39] M. Fabian, K.M.T. Yamada, J. Mol. Spectrosc. 198 (1999) 102–109.
[40] G. Baldacchini, F. D'Amato, G. Buffa, O. Tarrini, M. De Rosa, F. Pelagalli, J. Quant. Spectrosc. Radiat. Transfer 68 (2001) 625–633.
[41] A.S. Pine, M. Dang-Nhu, J. Quant. Spectrosc. Radiat. Transfer 50 (1993) 565–570.